Transient and Steady-State Dislocation Creep of Olivine Controlled by Dislocation Interactions at the Isostress Endmember

Wallis, David; Breithaupt, Thomas; Broerse, Taco

DOI
10.1029/2024JB030606

Publication date
2025

Document Version
Final published version

Published in
Journal of Geophysical Research: Solid Earth

Citation (APA)
Wallis, D., Breithaupt, T., & Broerse, T. (2025). Transient and Steady-State Dislocation Creep of Olivine Controlled by Dislocation Interactions at the Isostress Endmember. *Journal of Geophysical Research: Solid Earth*, *130*(6), Article e2024JB030606. https://doi.org/10.1029/2024JB030606

JGR Solid Earth

RESEARCH ARTICLE
10.1029/2024JB030606

Transient and Steady-State Dislocation Creep of Olivine Controlled by Dislocation Interactions at the Isostress Endmember

David Wallis[1], **Thomas Breithaupt**[1], **and Taco Broerse**[2]

[1]Department of Earth Sciences, University of Cambridge, Cambridge, UK, [2]Department of Geoscience and Remote Sensing, Delft University of Technology, Delft, the Netherlands

Abstract The rheological behavior of olivine deforming by dislocation creep controls geodynamic processes that involve steady-state flow or transient viscosity evolution. Longstanding rheological models applied to both contexts assume that dislocation creep of olivine aggregates occurs close to the isostrain endmember with each grain deforming to the same strain but supporting different stress. Here, we test this assumption by constructing isostrain and isostress models based on flow laws for single crystals and comparing them to rheological data from aggregates. This analysis reveals that strain rates measured on olivine aggregates agree with those predicted by the isostress model but are an order of magnitude faster than those predicted by the isostrain model. When extrapolated to conditions typical of the shallow upper mantle, the isostress model predicts steady-state viscosities that are one to three orders of magnitude less than those predicted by the isostrain model. Furthermore, deformation close to the isostress endmember implies that transient creep occurs predominantly by dislocation interactions, suggesting viscosity changes that are approximately one order of magnitude greater than those predicted previously based on grain interactions associated with the isostrain model.

Plain Language Summary Viscous flow of the hot rocks in Earth's upper mantle is a key process in the dynamic behaviors of the outer layers of the planet. The viscosity of these rocks is controlled primarily by that of the most abundant constituent mineral, which is olivine. Rocks composed of olivine have long been assumed to flow in a particular manner, whereby each grain undergoes the same shape change but supports a different stress due to interactions among neighboring grains. We test this assumption by predicting rates of flow using two models, in which neighboring grains are assumed either to interact or not to interact, and comparing them to rates of flow measured on olivine-rich rocks. This comparison reveals that olivine-rich rocks flow at the rates predicted by the model in which neighboring grains do not interact and therefore support the same stress but undergo different shape changes. This result overturns the aforementioned paradigm. Importantly, the flow behavior supported by our analysis is more complex than previous models and predicts more rapid flow in the aftermath of stress changes, such as those imposed by major earthquakes.

Key Points:

- Aggregates of coarse-grained olivine deform at strain rates predicted by the isostress model
- Transient dislocation creep of olivine is controlled by dislocation interactions
- Steady-state dislocation creep of olivine is controlled by the weakest, rather than the strongest, slip system

Supporting Information:

Supporting Information may be found in the online version of this article.

Correspondence to:

D. Wallis,
dw584@cam.ac.uk

Citation:

Wallis, D., Breithaupt, T., & Broerse, T. (2025). Transient and steady-state dislocation creep of olivine controlled by dislocation interactions at the isostress endmember. *Journal of Geophysical Research: Solid Earth*, *130*, e2024JB030606. https://doi.org/10.1029/2024JB030606

Received 14 NOV 2024
Accepted 20 MAY 2025

Author Contributions:

Conceptualization: David Wallis, Thomas Breithaupt, Taco Broerse
Data curation: David Wallis, Thomas Breithaupt, Taco Broerse
Formal analysis: David Wallis, Thomas Breithaupt, Taco Broerse
Funding acquisition: David Wallis
Investigation: David Wallis, Thomas Breithaupt, Taco Broerse
Methodology: David Wallis, Thomas Breithaupt, Taco Broerse
Project administration: David Wallis
Resources: David Wallis
Software: David Wallis, Thomas Breithaupt, Taco Broerse
Validation: David Wallis, Thomas Breithaupt, Taco Broerse
Visualization: David Wallis, Thomas Breithaupt, Taco Broerse

1. Introduction

The viscosity of Earth's upper mantle exerts a key control on the rates and styles of the majority of large-scale tectonic and geodynamic processes, including long-term convection and plate motion (e.g., Orowan, 1964; Tackley, 2000), short-term fault behavior (e.g., Freed, 2005), and glacial isostatic adjustment (e.g., Simon et al., 2022). Therefore, constraining the viscosity of the mantle and its evolution with strain is a major outstanding objective. The most direct estimates of the viscosities of Earth's upper mantle are derived from geodetic analyses of deformation induced by rapid changes in stress, such as those imposed by major earthquakes. Typically, geodetic measurements of surface displacements and gravity changes in the aftermath of an earthquake are used to constrain models of the spatiotemporal distribution of viscosity in the upper mantle (e.g., Broerse et al., 2015; Freed et al., 2012; Hoechner et al., 2011; Masuti et al., 2016; Muto et al., 2019). Notably, several such analyses indicate that viscosity depends nonlinearly on the applied stress, implying the activity of a dislocation-mediated deformation mechanism (e.g., Freed et al., 2006, 2012; Masuti et al., 2016). Such models also indicate that viscosity increases with time and strain after a stress change in a manner that cannot be accounted for using flow laws calibrated only for steady-state deformation (Freed et al., 2010, 2012; Masuti et al., 2016; Muto et al., 2019). This observation implies that the mantle undergoes transient creep, in which viscosity evolves during

Writing – original draft: David Wallis, Thomas Breithaupt, Taco Broerse
Writing – review & editing: David Wallis, Thomas Breithaupt, Taco Broerse

deformation due to changes in microstructure and micromechanical state, as is widely observed in laboratory experiments following changes in stress (e.g., Chopra, 1997; Hansen et al., 2021; Hanson & Spetzler, 1994; Post, 1977; Smith & Carpenter, 1987; Wiesman et al., 2024).

The accuracy of inferred mantle viscosities depends on the use of an appropriate rheological model for dislocation creep of olivine, which constitutes >60% of the upper mantle and therefore exerts the dominant control on its rheological properties (Zimmerman & Kohlstedt, 2004). As olivine exhibits pronounced elastic (Abramson et al., 1997) and viscous (Bai et al., 1991) anisotropy, modeling the deformation of an olivine aggregate is not straightforward. At pressures sufficiently high to prevent the opening of voids, successful models must maintain a compatible strain field among mechanically anisotropic grains. A compatible strain field could occur through either homogeneous or heterogeneous strain and these two possibilities lead to two endmember models, that is an isostrain endmember (Taylor, 1938) and an isostress endmember (Sachs, 1928). At the isostrain endmember, each grain deforms to the same strain. For viscous flow in three dimensions, this model imposes the constraint that each grain has the same strain and strain-rate tensors. If the grains are mechanically anisotropic, the isostrain model necessitates that grains with different lattice orientations support different stresses. In contrast, at the isostress endmember, each grain is subject to the same stress tensor applied to the bulk material. In this case, mechanical anisotropy dictates that grains with different lattice orientations deform to different strains at different strain rates. Strain compatibility between grains can then be facilitated by intragranular strain heterogeneity, whereby spatial gradients in plastic strain arise within grains (Ashby, 1970; Paterson, 1969). These intragranular strain gradients are maintained by the presence of geometrically necessary dislocations (Fleck et al., 1994). The isostrain and isostress endmember models make significantly different predictions about the nature of transient creep and steady-state flow.

The isostrain model was first considered in detail for Earth materials in relation to early experiments on water ice (Ashby & Duval, 1985). In the isostrain model, transient creep occurs due to grain interactions that transfer stress between two sets of grains with different crystallographic orientations (Karato, 1998, 2021; Masuti & Barbot, 2021). In anisotropic crystal structures, such as ice and olivine, the slip systems upon which dislocations glide can have viscosities that differ by orders of magnitude (Bai et al., 1991; Duval et al., 1983). At the beginning of deformation, dislocation glide is assumed to occur at the fastest rate in grains with orientations that result in high resolved shear stress on the weakest slip system. However, to maintain strain compatibility among adjacent grains, this initial deformation progressively transfers stress to grains in which the weakest slip system has low resolved shear stress. This transfer of stress is assumed to activate stronger slip systems in the latter set of grains, with the strain rate on the strongest slip system controlling the steady-state strain rate of the aggregate. The transition from the bulk strain rate initially being controlled by the weak slip system to later being controlled by the strong slip system results in a strain-hardening transient. As the steady-state strain rate at this endmember is limited by the strain rate on the strongest slip system, this model provides an upper bound on the strength of the aggregate.

In contrast, in the isostress model each grain behaves as a single crystal subject to the same stress tensor. In this case, the steady-state strain rate of an aggregate is typically dominated by deformation on the easy slip system such that the isostress model predicts an aggregate to be weaker than predicted by the isostrain model. Furthermore, in the absence of intergranular stress transfer, any transient creep must arise from intragranular processes. In the case of olivine, the dominant intragranular process appears to be elastic interactions among dislocations (Hansen et al., 2021; Wallis et al., 2017, 2021, 2022). This inference is based on recent deformation experiments and microstructural observations of olivine single crystals deformed at room temperature (Hansen et al., 2019) and temperatures in the range 1,200–1,300°C (Hansen et al., 2021; Wallis et al., 2017, 2021). Following reductions in stress, single crystals of olivine undergo time-dependent reverse strains (Hansen et al., 2021). This reverse deformation reveals the existence of a back stress within the material that counteracts the applied stress and is inferred to arise from elastic interactions among dislocations (Hansen et al., 2021). As dislocation density changes during deformation, so does the intensity of the elastic interactions among dislocations that resist dislocation motion (Hansen et al., 2021; Wallis et al., 2021). The increasing elastic interactions and associated back stress counteract the applied stress, leading to a strain-hardening transient (Hansen et al., 2021). We note that dislocations impart significant intragranular stress heterogeneity to both single crystals (Hansen et al., 2021; Wallis et al., 2017) and aggregates (Wallis et al., 2021) of olivine, which causes elastic interactions that generate back stress. However, to be clear, the term “isostress” refers to a lack of systematic

differences in grain-average stress supported by grains with different lattice orientations regardless of intragranular stress heterogeneity over length scales smaller than the grain size.

Deformation of olivine aggregates has long been considered to occur close to the isostrain endmember (Hansen et al., 2016; Karato, 1998, 2021; Masuti & Barbot, 2021; Masuti et al., 2019). This inference is based primarily on the observation that steady-state strain rates measured on aggregates lie among the strain rates measured on single crystals oriented to activate the strong slip systems (Chopra & Paterson, 1984; Keefner et al., 2011; Mei & Kohlstedt, 2000). This observation has been taken to indicate that the strong slip systems have been activated in the aggregates and become rate limiting due to grain interactions (Karato, 1998, 2021). This analysis is often justified on the basis of the von Mises criterion, which states that five independent slip systems are required to allow a crystal to deform to an arbitrary strain by dislocation glide (von Mises, 1913). However, olivine lacks five independent slip systems and therefore strain-producing mechanisms other than dislocation glide must also operate in the isostrain model (Paterson, 1969). Despite the operation of these alternative mechanisms, it is likely that the strongest of the available slip systems still limits the bulk strain rate under isostrain conditions depending on the relative efficiency of each mechanism. The isostrain interpretation has provided the conceptual basis for recent geodetic analyses employing nonlinear adaptations of the Burgers model, in which the two viscous elements represent the weak slip system, which controls the initial transient strain rate, and the strong slip system, which controls the strain rate at steady state (Masuti & Barbot, 2021; Masuti et al., 2016; Muto et al., 2019). Such formulations are typically parameterized using flow laws for individual slip systems calibrated at steady state (Masuti et al., 2016; Muto et al., 2019).

Here, we query the relevance of all three of these aspects of the isostrain interpretation. First, we contend that previous face-value comparisons between strain rates measured on aggregates and those measured on single crystals are invalid because the resolved shear stresses on each slip system (i.e., the shear stress acting on the slip plane in the slip direction) averaged over all grains in an aggregate are less than those in experiments on single crystals that are oriented to maximize the resolved shear stresses acting on particular slip systems. That is, even if grains do not interact, aggregates will deform at slower strain rates than single crystals oriented to activate the easy slip system due simply to differences in resolved shear stress. Therefore, we pose the null hypothesis that, once the resolved shear stresses acting on each slip system are properly accounted for, steady-state dislocation creep of coarse-grained aggregates of olivine occurs at the strain rates expected of an ensemble of grains that do not interact by intergranular stress transfer, that is, at the strain rates predicted by the isostress model. Second, we note that the von Mises criterion in a strict sense neglects the potential for intragranular strain heterogeneity or strain-producing processes other than dislocation glide (Goetze, 1978; Paterson, 1969), both of which are ubiquitous in deforming olivine aggregates and potentially reduce the impact of the strong slip system on the bulk strain rate. Lastly, we emphasize that single crystals with no neighboring grains exhibit marked transient creep (Cooper et al., 2016; Durham & Goetze, 1977; Durham et al., 1979; Hansen et al., 2021; Hanson & Spetzler, 1994; Kohlstedt & Goetze, 1974), which must arise from intragranular processes. As the same intragranular processes must also operate within grains in aggregates, intergranular stress transfer in the isostrain model is at best an incomplete description of transient creep. Thus, models of transient creep based on steady-state flow laws for the soft and hard slip systems (Masuti & Barbot, 2021; Masuti et al., 2016; Muto et al., 2019) are missing an important set of intragranular physical processes.

To test our null hypothesis, we compare predicted strain rates from isostress and isostrain models based on flow laws for each slip system measured on single crystals to strain rates measured on aggregates at steady state. Furthermore, we compare strain rates measured on aggregates at the start of deformation prior to any hardening to a recently calibrated flow law that can predict strain rates in the absence of intragranular hardening. This comparison allows us to explore the extent to which either steady-state strain rates are controlled by the strong slip system and transients arise from grain interactions (i.e., the isostrain model) or steady-state strain rates are dominated by the weak slip system and transients arise from intragranular processes (i.e., the isostress model). We then explore the implications of discriminating between the isostrain and isostress models for deformation in the steady-state and transient regimes under natural conditions.

2. Methods

2.1. Experimental Materials

To compare the strain rates of aggregates of olivine to those expected from combinations of individual slip systems, the experimental data sets must be carefully selected to properly control for the full range of variables that can influence steady-state strain rates. These variables include composition, grain size, temperature, pressure, oxygen fugacity, the activities of H_2O and SiO_2, and the presence or absence of partial melt (Bai et al., 1991; Keefner et al., 2011; Warren & Hansen, 2023). For aggregates of olivine, we work primarily with the rheological data measured in the experiments of Keefner et al. (2011) on Åheim dunite, a rock consisting of approximately 95% olivine. These experiments are particularly appropriate because the coarse grain size of 0.9 mm of the dunite prevents significant contributions from deformation mechanisms other than dislocation creep and because these experiments were conducted under carefully controlled oxygen fugacities. These samples were predried, had the activity of silica buffered by the presence of small amounts of orthopyroxene, and lacked microstructural evidence for the presence of partial melt. Keefner et al. (2011) recorded strain rates after steady state was achieved at each load step, which was typically attained after a strain of $\lesssim$0.5% at each load. In analyzing this relatively pure and coarse-grained material we deliberately eliminate some effects and processes that potentially modify viscosity in other rocks, such as the effects of secondary phases, grain-size evolution, dislocation-accommodated grain-boundary sliding, and diffusion creep. Rather than trying to simulate all processes that can affect the viscosity of mantle rocks, our aim is to provide a focussed test of fundamental isostress or isostrain behavior in coarse-grained aggregates of olivine.

In addition to the mechanical data obtained at steady state and published by Keefner et al. (2011), we include one new datum from their experiments obtained from their original mechanical data. This datum was taken over the first 0.25% plastic strain during the first load step on sample PI-1166 at a temperature of 1,250°C, differential stress of 258 MPa, and strain rate of 8×10^{-5} s^{-1} with oxygen fugacity at the nickel-nickel oxide buffer. The raw data of load and displacement were converted to stress and strain taking into account the instantaneous sample dimensions and the strength of the jacketing materials following Keefner et al. (2011). This particular experiment was conducted at the same temperature and oxygen fugacity as those of the experiments of Hansen et al. (2021) that were used to benchmark the model of Breithaupt et al. (2023), against which this datum is compared. The other experiments of Keefner et al. (2011) at this temperature and oxygen fugacity did not have useable mechanical data for the relevant portion of each experiment.

We also use data from samples 4392, 4462, and 4526 from selected experiments by Chopra and Paterson (1981, 1984) and Doukhan et al. (1984) that were deformed at temperatures and oxygen fugacities that are useful in making comparisons to the data of Keefner et al. (2011) and the flow law for dislocation glide in the absence of hardening (Breithaupt et al., 2023). These samples also consisted of either Åheim or Anita Bay dunite that was predried and in which the silica activity was again buffered by orthopyroxene. However, in these experiments the oxygen fugacity is less well constrained than in the experiments of Keefner et al. (2011). Sample 4392 may have retained residual hydrous defects (Chopra & Paterson, 1984), and sample 4526 displayed glassy films on grain boundaries that suggest the presence of small fractions of partial melt (Doukhan et al., 1984). These factors provide potential explanations for why the steady-state strain rates in these experiments are slightly faster than those in the experiments of Keefner et al. (2011). As these experiments were conducted at constant strain rates, we picked the stress at the onset of plastic deformation (i.e., the yield stress) before any strain hardening had occurred and the stress during steady-state flow after strain hardening.

To represent the strain rates on individual slip systems at steady state, we use the flow laws of Bai et al. (1991). These flow laws were derived from uniaxial experiments performed on single crystals of dry San Carlos olivine with the oxygen fugacity carefully controlled during the experiments. We use the flow laws from experiments in which the silica activity was set by the presence of orthopyroxene on the surface of the sample. These factors make the flow laws of Bai et al. (1991) the most suitable upon which to formulate comparisons to the data from olivine aggregates by Keefner et al. (2011) for the purpose of steady-state flow. Notably, as these flow laws were calibrated at steady state after the initial transients, they intrinsically include the effects of intragranular hardening by dislocation interactions. Moreover, having been calibrated on single crystals, these flow laws naturally omit intergranular hardening by stress transfer among grains.

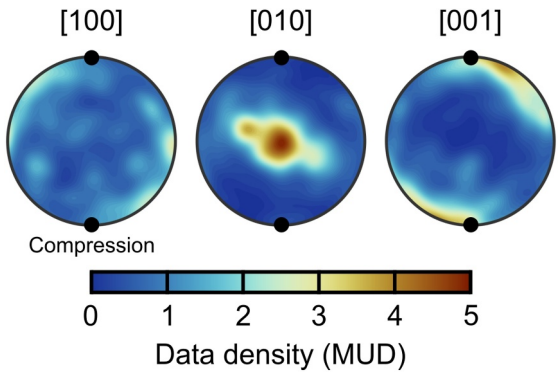

Figure 1. The crystallographic preferred orientation of Åheim dunite used in the experiments of Keefner et al. (2011) and as input to the isostress and isostrain models. Black dots indicate the direction of maximum principle stress applied in the experiments and models. The color scale is in multiples of uniform distribution based on the average orientation of each grain.

In contrast, to calculate strain rates at the onset of deformation before any hardening, we use the flow law of Breithaupt et al. (2023) for dislocation glide at high temperatures. This flow law was calibrated on data collected at steady state in experiments performed on aggregates by Hansen et al. (2011) and Keefner et al. (2011), as part of a wider inversion for both dislocation-glide and dislocation-recovery parameters. The silica activity in these experiments was buffered by the presence of small amounts of orthopyroxene. Only experiments in which the oxygen fugacity was controlled at the nickel-nickel oxide buffer were used in the calibration. The flow law has been demonstrated to well predict transient creep of single crystals deformed under oxygen fugacities controlled at the nickel-nickel oxide buffer in stress-reduction experiments (Hansen et al., 2021). Variation in oxygen fugacity has not yet been demonstrated to impact transient strain rates limited by dislocation glide, and thus, we do not correct for variation in oxygen fugacity when comparing the flow law for dislocation glide calibrated at the nickel-nickel oxide buffer to transient strain rates measured at the iron-wüstite buffer. Instead, this comparison provides an initial test for any effect of oxygen fugacity on rates of dislocation glide.

The remaining variables to consider across the sample sets are composition and pressure. San Carlos olivine (Jin et al., 1994), Åheim dunite (Chopra & Paterson, 1981; Keefner et al., 2011), and Anita Bay dunite (Chopra & Paterson, 1981) all have Mg/(Mg + Fe) in the range 0.89–0.93 and are therefore similar in major-element chemistry. Differences in major- and trace-element chemistry of the magnitudes present between, for example, San Carlos and Åheim olivine, do not generate significant differences in creep rates and dependencies under the conditions of interest (Jin et al., 1994). The experiments on single crystals were conducted at a confining pressure of 0.1 MPa (Bai et al., 1991) whereas those on dunites were conducted at a confining pressure of 300 MPa (Chopra & Paterson, 1981, 1984; Doukhan et al., 1984; Keefner et al., 2011). The effect of pressure (Dixon & Durham, 2018) on dislocation creep of aggregates of dry olivine over this pressure difference is only factor of approximately 1.4 in strain rate, which we account for in the models as described below.

2.2. Electron Backscatter Diffraction

We measured the crystallographic preferred orientation (CPO) of Åheim dunite, which was used as starting material for the experiments of Keefner et al. (2011), on a piece supplied by the Rock and Mineral Physics Laboratory, University of Minnesota. The sample was cut parallel to the foliation, polished with progressively finer diamond grits, and finished with colloidal silica. We acquired orientation measurements by electron backscatter diffraction (EBSD) on an FEI Quanta 650 field emission gun environmental scanning electron microscope in the Department of Earth Sciences, University of Oxford, equipped with an Oxford Instruments AZtec acquisition system and Nordlys Nano EBSD detector. The map consists of 808 × 346 data points at a step size of 10 μm and covers approximately one third of the cross-sectional area of the samples used by Keefner et al. (2011). Misindexed pixels that differed in orientation from their neighbors by >10° were removed and unindexed pixels surrounded by >6 neighbors within the same grain were iteratively assigned the average orientation of their neighbors. The resulting data set consists of the average orientation of each of the resulting 418 grains. Figure 1 presents the CPO of our sample. This CPO is near identical to that plotted in Figure 8 of Keefner et al. (2011), both in terms of the topologies of the distributions and the strengths of the distributions quantified as multiples of uniform distribution. This similarity provides confidence that the CPO of the Åheim dunite is homogeneous and therefore that the measured CPO is representative of that used in the deformation experiments of Keefner et al. (2011). We used the CPO of the undeformed Åheim dunite that was used as starting material for the experiments (Keefner et al., 2011) in our calculations for the isostress and isostrain models. We modeled compression of the dunite with the maximum principal stress in the same direction relative to the CPO as was applied in the experiments of Keefner et al. (2011).

2.3. Models of Steady-State Deformation

2.3.1. Isostress Model for Steady-State Deformation

To model the isostress endmember strain rate of an olivine aggregate, we utilize the approach of Tielke et al. (2016) and Meyers and Kohlstedt (2021), which is a simple formulation of the classical isostress model of Sachs (1928). In this conceptual end-member model for the deformation of an aggregate of grains, each grain is assumed to be subject to the same local stress tensor, which is the macroscopic stress tensor applied to the bulk material. Therefore, this approach does not model stress heterogeneity arising from transfer of stress between grains. We note that in detail stress heterogeneity is present within deformed olivine aggregates due to the stress fields of dislocations (Hansen et al., 2021; Wallis et al., 2017, 2020, 2021). However, these stresses are also present in deformed single crystals (Wallis et al., 2017, 2020) and result from a different set of physical processes compared to intergranular stress transfer. Specifically, the stress heterogeneity imparted by dislocations controls intragranular hardening by long-range dislocation interactions (Hansen et al., 2021; Wallis et al., 2017, 2020, 2021), the presence or absence of which we account for in the flow laws input to the model (Bai et al., 1991; Breithaupt et al., 2023) as described below. Therefore, in using the term "isostress model," we refer specifically to a lack of systematic differences in the average stress tensor supported by subpopulations of grains with different crystallographic orientations. The benefit of this minimalist model is that it can test the extent to which strain rates measured on olivine aggregates can be explained simply by resolving the stress tensor applied to the bulk rock onto the slip systems in each grain in the absence of other confounding physical processes.

The modeling procedure is based on the computation of stresses and strain rates in both the sample and crystallographic reference frames (Tielke et al., 2016). We define the deviatoric stress tensor, $\boldsymbol{\sigma}$, in the sample reference frame, making it consistent with the loading axis applied experimentally to the Åheim dunite and the grain orientations within. The deviatoric stress tensor is rotated into the crystallographic reference frame (indicated by the prime symbol) of each grain by

$$\boldsymbol{\sigma}' = \mathbf{R}\boldsymbol{\sigma}\mathbf{R}^{\mathrm{T}}, \tag{1}$$

where $\mathbf{R}$ is the passive rotation matrix defining the rotation from the crystal reference frame to the sample reference frame. Slip systems, α, are defined by their unit Burgers vector, $\mathbf{b}$, and unit slip-plane normal, $\mathbf{n}$. We consider the (010)[100], (001)[100], (100)[001], and (010)[001] slip systems (Bai et al., 1991). The resolved shear stress on each slip system, τ^{α}, is calculated by

$$\tau^{\alpha} = \boldsymbol{\mu}^{\alpha} : \boldsymbol{\sigma}', \tag{2}$$

where $\boldsymbol{\mu}^{\alpha}$ is the symmetric Schmid tensor determined as

$$\boldsymbol{\mu}^{\alpha} = \frac{1}{2}(\mathbf{b}^{\alpha} \otimes \mathbf{n}^{\alpha} + \mathbf{n}^{\alpha} \otimes \mathbf{b}^{\alpha}), \tag{3}$$

where $\otimes$ is the tensor outer product. The corresponding differential stress, σ^{α}, acting on each slip system is calculated as

$$\sigma^{\alpha} = |2\tau^{\alpha}|, \tag{4}$$

Then, we determine the strain rate, $\dot{\varepsilon}^{\alpha}$, due to dislocation motion on each slip system using the flow laws for single crystals of San Carlos olivine. To calculate strain rates during steady-state flow, inherently capturing the effects of intragranular hardening during the preceding transient, we use the flow laws of Bai et al. (1991), following the general form

$$\dot{\varepsilon}^{\alpha} = \dot{\varepsilon}^{\alpha}\left(\sigma^{\alpha}, T, P, f_{\mathrm{O}_2}\right) \mathrm{sgn}(\tau^{\alpha}), \tag{5}$$

where f_{O_2} is oxygen fugacity. We use the three flow laws for single crystals of olivine with the silica activity buffered by orthopyroxene and that were deformed in different orientations chosen to activate the slip systems

listed above. As the (001)[100] and (100)[001] slip systems are activated simultaneously in experiments on a single crystal orientation and always have the same Schmid factor, we calculate their combined strain rate using a single flow law (Bai et al., 1991). Here, the effect of pressure, P, is added to the original flow laws by incorporating more recent estimates of the activation volume, ΔV, for single crystals deformed in each orientation (Raterron et al., 2012). Specifically, the slip-system specific activation energies are adjusted with the relevant activation volume as

$$Q(P) = Q_{\text{ref}} + (P - P_{\text{ref}})\Delta V, \tag{6}$$

where Q_{ref} is the fitted activation energy at the reference pressure $P_{\text{ref}} = 0.1$ MPa, which corresponds to the pressures at which the flow laws of Bai et al. (1991) were calibrated. This pressure effect is small in that, for example, it reduces strain rates predicted by the isostress model at a pressure of 300 MPa by approximately 30% relative to those predicted at a pressure of 0.1 MPa. The corresponding shear strain rates, $\dot{\gamma}^{\alpha}$, are

$$\dot{\gamma}^{\alpha} = 2\dot{\varepsilon}^{\alpha}, \tag{7}$$

which can be summed across slip systems to give the strain-rate tensor of each grain in the crystallographic reference frame as

$$\dot{\boldsymbol{\varepsilon}}' = \sum_{\alpha=1}^{3} \boldsymbol{\mu}^{\alpha}\dot{\gamma}^{\alpha}. \tag{8}$$

This strain-rate tensor is rotated into the sample reference frame, giving $\dot{\boldsymbol{\varepsilon}}_{\text{grain}}$, by

$$\dot{\boldsymbol{\varepsilon}}_{\text{grain}} = \mathbf{R}^{\mathrm{T}}\dot{\boldsymbol{\varepsilon}}'\mathbf{R}. \tag{9}$$

Assuming as a simple approximation that each grain has the same volume, we estimate the strain rate of the aggregate by taking the arithmetic mean of $\dot{\boldsymbol{\varepsilon}}_{\text{grain}}$ across all grains. Finally, we take the component of the strain rate of the aggregate that is parallel to the applied loading axis.

2.3.2. Isostrain Model for Steady-State Deformation

We contrast our calculations of the isostress endmember with calculations assuming isostrain, the alternative conceptual end-member model for the deformation of aggregates (Taylor, 1938). In the isostrain limit, each grain is subject to the same macroscopic strain tensor. Due to plastic anisotropy, each grain possesses its own local stress tensor. The macroscopic stress tensor then corresponds to an average of all of the grain-specific local stress tensors. Application of the isostrain model to olivine is challenging because olivine does not possess sufficient independent slip systems to produce an arbitrary strain tensor (Paterson, 1969). Previous studies have addressed this issue by incorporating stronger fictitious slip systems (Tommasi et al., 2000) or by partially relaxing the isostrain assumption to require the grain-specific strain tensor to closely match, rather than exactly match, the macroscopic strain tensor (Hansen et al., 2016). If stronger fictitious slip systems are introduced, the modeled aggregate behavior may be strengthened by an arbitrary amount depending on the assumed strength of the fictitious slip system (Castelnau et al., 2008). Alternatively, if the isostrain assumption is partially relaxed, alternative unmodelled deformation processes are implicitly assumed to operate that would allow each grain to completely fulfill the isostrain condition. These unmodelled deformation processes are assumed to have negligible strength. In this work, we instead take inspiration from published isostrain models of transient creep that neglect the tensorial aspects of deformation and instead assume a scalar formulation of isostrain (Ashby & Duval, 1985; Karato, 1998, 2021). We focus on the component of strain in the compression direction and enforce the isostrain condition on this component only. We note that enforcing the isostrain condition on all components will likely strengthen the modeled aggregate behavior, and thus, the predicted strain rates provide upper bounds on those that would be predicted by more complex isostrain approaches.

We define the grain-specific, one-dimensional flow law to be

$$\dot{\varepsilon}_i = A_i\sigma_i^n, \tag{10}$$

where the subscript indicates that a property is specific to the ith grain, n is the stress exponent taken to be equal to 3.5 for all grains (Bai et al., 1991), and A_i is a grain-specific flow-law parameter. That A_i is variable among grains reflects that each grain has a different crystallographic orientation.

In the isostrain limit, at steady-state, each grain experiences the bulk plastic strain rate $\dot{\varepsilon}_{\text{isostrain}}$. The grain-specific stress is therefore given by

$$\sigma_i = \dot{\varepsilon}_{\text{isostrain}}^{1/n} A_i^{-1/n}. \tag{11}$$

In the alternative isostress limit, all grains are subject to the macroscopic stress $\sigma_i = \sigma$. Thus, we can determine the grain-specific flow-law constants by

$$A_i = \dot{\varepsilon}_{i,\text{isostress}} \sigma^{-n}, \tag{12}$$

where $\dot{\varepsilon}_{i,\text{isostress}}$ are the grain-specific strain rates in the compression direction determined using the isostress methodology detailed above.

The macroscopic stress is determined by the average of the grain-specific stresses. Taking the average of Equation 12, and substituting Equation 11, we find

$$\sigma = \dot{\varepsilon}_{\text{isostrain}}^{1/n} \frac{1}{N} \sum_{i=1}^{N} \sigma \dot{\varepsilon}_{i,\text{isostress}}^{-1/n}, \tag{13}$$

where N is the total number of grains. Here, we make the assumption again that each grain has the same volume. We then divide by the macroscopic stress and rearrange to find the steady-state plastic strain rate under the isostrain model

$$\dot{\varepsilon}_{\text{isostrain}} = \left(\frac{1}{N} \sum_{i=1}^{N} \dot{\varepsilon}_{i,\text{isostress}}^{-1/n} \right)^{-n}. \tag{14}$$

2.4. Models of Viscosity Evolution

To model viscosity evolution during transient creep, we employ the models Karato (2021) and Breithaupt et al. (2023), which are based on grain interactions and dislocation interactions respectively. Breithaupt et al. (2023) provide a model for the temporal evolution of strain rate resulting from changes in the density of dislocations and the strength of interactions among them. In contrast, Karato (1998, 2021) proposed a model for the evolution of strain rate based on transfer of stress from the weakest slip system to a stronger slip system due to grain interactions. We perform a simple comparison of the behaviors of these models to demonstrate that they differ significantly for applications to geodynamic questions.

2.4.1. Model of Intergranular Hardening by Grain Interactions

The model of intergranular hardening by grain interactions proposed by Karato (2021) assumes a coupled system of a weak and a strong slip system. Following a stress increase, the initial increment of deformation occurs on the weak slip system in grains with orientations that provide this slip system with high resolved shear stress. Progressive deformation transfers stress from this weak slip system to stronger slip systems that are activated to maintain a homogeneous strain field without strain incompatibilities at grain boundaries. Consequently, the initial increment of deformation is controlled by the viscosity of the weak slip system whereas eventual steady-state flow is controlled by the viscosity of the strong slip system. Different from the original analysis of Karato (2021), we assume a pre-stressed material by applying a background stress (in the same direction as the stress increase) that results in an existing transfer of stress up to a converged state that is present prior to the application of a new constant stress. The model assumes steady-state deformation of each slip system so that the viscosities of individual slip systems do not evolve with strain or time. We use the pressure-adjusted flow laws for individual slip systems from Bai et al. (1991), namely the weak (010)[100] and strong (010)[001] slip systems.

In the model of grain interactions (Karato, 2021), strain rate depends of the difference between the applied differential stress, σ, and the transferred stress, S, which defines effective stresses, σ_1 and σ_2 acting on the weak and strong slip systems, respectively, as

$$\sigma_1 = \sigma - S_1 \text{ and } \sigma_2 = \sigma - S_2, \tag{15}$$

with the condition that

$$S_1 = -S_2 \tag{16}$$

to achieve a net transferred stress of zero. The strain rate for each slip system then becomes a function of the effective stresses, σ_1 and σ_2, of the form

$$\dot{\varepsilon}_{1,2} = f\left(\sigma_{1,2}, A, f_{O_2}^m, \exp\left(\frac{-Q}{RT}\right)\right), \tag{17}$$

with pre-exponent A, stress exponent n, oxygen fugacity f_{O_2} with exponent m, activation energy Q, ideal gas constant R, and absolute temperature T.

The constitutive equations from Bai et al. (1991) incorporate multiple mechanisms that are active concurrently or sequentially and were inferred to represent the effects of different microphysical processes in limiting rates of dislocation motion over different ranges of thermodynamic conditions (Table 4 of Bai et al., 1991 and their discussion thereof). Each of these mechanisms separately follow a power-law flow law of the form

$$\dot{\varepsilon} = A\sigma^n f_{O_2}^m \exp\left(\frac{-Q}{RT}\right). \tag{18}$$

For the weak slip system, (010)[100], the constitutive equation includes three mechanisms, a, b, and c, with mechanisms b and c operating sequentially, while this combination acts concurrently with mechanism a as

$$\dot{\varepsilon}_1 = \dot{\varepsilon}_a + \left(\dot{\varepsilon}_b^{-1} + \dot{\varepsilon}_c^{-1}\right)^{-1}. \tag{19}$$

The strong slip system, (010)[001], consists of two concurrent mechanisms, d and e, which lead to the constitutive equation

$$\dot{\varepsilon}_2 = \dot{\varepsilon}_d + \dot{\varepsilon}_e. \tag{20}$$

We compute oxygen fugacity, f_{O_2}, as a function of temperature and pressure at the FMQ buffer (Ballhaus et al., 1991; B. R. Frost, 1991; O'Neill, 1987a, 1987b). Table S1 in Supporting Information S1, contains the values of the parameters for each mechanism that we use in the model of grain interactions.

The resulting strain rate of the coupled system is (Equation 14 of Karato (2021))

$$\dot{\varepsilon} = \frac{1}{2}(\dot{\varepsilon}_1 + \dot{\varepsilon}_2). \tag{21}$$

To maintain homogeneous strain, the time derivative of transferred stress is (Equation 17 of Karato (2021))

$$\dot{S}_1 = \frac{\mu}{2}(\dot{\varepsilon}_1 - \dot{\varepsilon}_2), \tag{22}$$

where μ is the shear modulus. We integrate the transferred stress rate, taking small time steps, and subsequently use the updated effective stress to calculate a new strain rate, until we reach steady-state strain rates.

2.4.2. Model of Intragranular Hardening by Dislocation Interactions

We use the model of intragranular hardening from Breithaupt et al. (2023) to model strain rates by dislocation creep as a function of the difference between the applied stress, σ, and an internal back stress, σ_b, following

$$\dot{\varepsilon} = A \exp\left(\frac{-Q}{RT}\right)\sigma_\rho^2 \sinh\left(\frac{\sigma - \sigma_b}{\sigma_{ref}(T)}\right), \tag{23}$$

were A is a pre-exponential constant and Q is the pressure-adjusted activation energy (see Equation 6). Breithaupt et al. (2023) decompose the back stress into a Taylor stress, σ_ρ, resulting from dislocation interactions and a threshold stress, σ_d, that describes the stress necessary to expand a dislocation loop within a grain of a particular size such that

$$\sigma_b = \sigma_\rho + \sigma_d, \tag{24}$$

where the Taylor stress relates to the scalar dislocation density, ρ, as

$$\sigma_\rho = \alpha \mu b \sqrt{\rho}, \tag{25}$$

where α is a constant, μ is the shear modulus, and b is the magnitude of the Burgers vector. The threshold stress is defined as

$$\sigma_d = \beta \mu b / d, \tag{26}$$

where β is a constant and d is grain size. The effective stress is scaled by a temperature-dependent reference stress, defined as

$$\sigma_{ref}(T) = \sigma_P^* \frac{RT}{Q}, \tag{27}$$

where σ_P^* is the strength of local barriers to dislocation motion, and Q is the pressure-adjusted activation energy.

In this model, transient behavior results from the evolution of dislocation density by processes that increase (storage) or decrease (recovery) the dislocation density. Breithaupt et al. (2023) account for dynamic dislocation storage due to dislocation glide and account for static recovery facilitated by pipe diffusion and grain-boundary diffusion. As the Taylor stress is dependent on dislocation density, the effective stress changes as the dislocation density evolves. Breithaupt et al. (2023) account for the effect of changing dislocation density in the evolution of the Taylor stress (their Equation 29) by

$$\dot{\sigma}_\rho = M\left(\frac{\sigma_\rho + \sigma_d}{\sigma_\rho}\dot{\varepsilon} - \mathcal{R}_{gb}(T)\sigma_\rho^3 \sigma_d - \mathcal{R}_{pipe}(T)\sigma_\rho^5\right), \tag{28}$$

where M is the plastic modulus, which controls the overall rate of the transient. $\mathcal{R}_{gb}(T)$ and $\mathcal{R}_{pipe}(T)$ are rate coefficients for static recovery by grain-boundary diffusion and pipe diffusion, respectively, defined as

$$\mathcal{R}_{gb}(T) = \mathcal{R}_{gb}^* \exp\left(\frac{-Q}{RT}\right) \tag{29}$$

and

$$\mathcal{R}_{pipe}(T) = \mathcal{R}_{pipe}^* \exp\left(\frac{-Q}{RT}\right), \tag{30}$$

where $\mathcal{R}^*_{gb}$ and $\mathcal{R}^*_{pipe}$ are pre-exponential constants for grain-boundary diffusion and pipe diffusion, respectively, and Q is the pressure-adjusted activation energy. We start with a dislocation density that conforms to the steady-state value for the initial background stress and update the Taylor stress at each time step and use this value to compute a new strain rate. The values of the parameters that we use in the model of dislocation interactions are given in Table S2 in Supporting Information S1.

3. Results

Figures 2a and 2b present comparisons of steady-state strain rates (normalized to two different temperatures and oxygen fugacities) measured from dunite by Keefner et al. (2011) to those predicted by the isostress and isostrain models. In these figures, the power-law flow law for dunites of Keefner et al. (2011), which was originally fit to the experimental data, is plotted in blue for comparison. The solid black lines indicate strain rates predicted by this isostress model based on the flow laws of Bai et al. (1991), adjusted to incorporate more recently calibrated pressure effects (Raterron et al., 2012), for each slip system. The heavy line is calculated using the CPO of the dunite (Figure 1) whereas the fine line (which overlaps the solid line in Figure 2b) is calculated based on 10^5 random crystal orientations lacking a CPO. As these flow laws were calibrated on single crystals at steady state after the initial transients, they intrinsically include the effects of intragranular hardening by dislocation interactions. Strikingly, the steady-state strain rates predicted by the isostress model are in excellent agreement with the data measured on dunite across the full range of differential stresses. Compared to the strain rates predicted based on random crystal orientations, those predicted based on the CPO of the dunite give a slightly better fit to the experimental data and a closer match to the flow law of Keefner et al. (2011), but this effect of CPO is minimal and the match is good in both cases. Figure 2c presents the contributions of different slip systems to the total strain rate in the isostress model with the CPO of the dunite, and reveals that the weakest slip system, (010)[100], contributes most to the strain rate whilst the strongest slip system, (010)[001], contributes about two orders of magnitude less to the total strain rate. The agreement between the total strain rates predicted by the isostress model and those measured in experiments indicates that dunites deform at the strain rates expected of an ensemble of grains that do not mechanically interact by systematic, orientation-dependent stress transfer. In contrast, steady-state strain rates predicted by the isostrain model based upon the same single-crystal flow laws, indicated by the dashed black lines, are approximately an order of magnitude slower than those measured in the experiments. Again, this is true for strain rates predicted based either on the CPO of the dunite, indicated by the thick dashed line, or random orientations, indicated by the fine dashed line. The slow strain rates predicted by the isostrain model result from stress transfer from the easy slip system to the strong slip system. Overall, the magnitudes of steady-state strain rates measured in experiments are in good agreement with predictions of the isostress model and poor agreement with predictions of the isostrain model.

The success of the isostress model is broadly consistent with the outcome of similar analysis of mechanical and microstructural data obtained on dunite from the Josephine peridotite by Meyers and Kohlstedt (2021). The strain rates that they predicted from the isostress model were similar to, but slightly faster than, those measured in their experiments. The closer agreement between modeled and measured strain rates in our analysis (Figure 2) compared to that of Meyers and Kohlstedt (2021, their Figure 7) potentially stems from the more homogeneous composition and microstructure of Åheim dunite relative to those of Josephine dunite.

In addition to analyzing the magnitudes of the strain rates predicted by the isostress and isostrain models, we also examine their predicted dependencies on oxygen fugacity and temperature in Figure 3. The isostress and isostrain models predict different dependencies of strain rate on oxygen fugacity and temperature due to the different dependencies of the individual slip systems on these variables (Bai et al., 1991). The data plotted in orange and purple in Figure 3 were collected at the nickel-nickel oxide and iron-wüstite buffers respectively and the separation between them indicates the oxygen-fugacity dependence of the steady-state strain rate. The oxygen-fugacity dependence of the strain rate predicted by the isostress model, indicated by the separation between the orange and purple solid lines, is in reasonable agreement with that exhibited by the measured strain rates (Keefner et al., 2011). For comparison, the conventional power-law flow law (Keefner et al., 2011) originally fit to the experimental data is indicated by the dot-dashed lines and exhibits a similar separation between the curves for different oxygen fugacities to that predicted by the isostress model. In contrast, the oxygen-fugacity

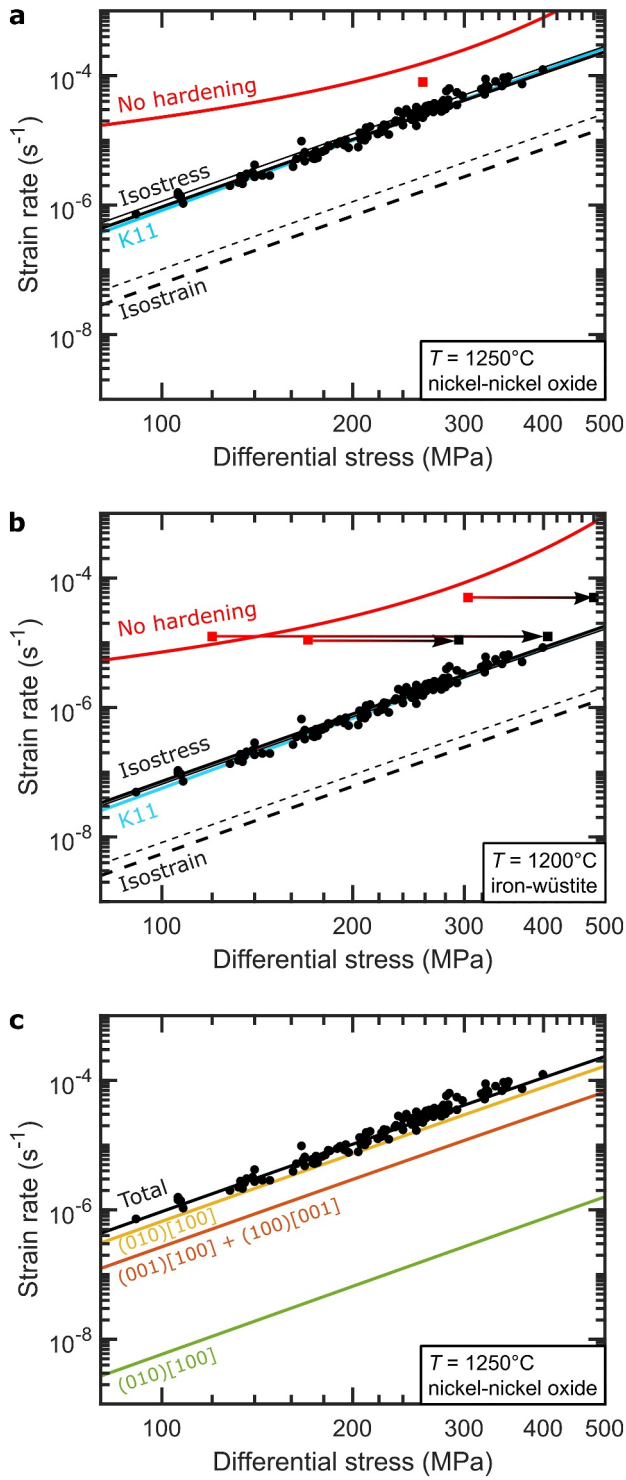

Figure 2.

dependence of strain rate predicted by the isostrain model, indicated by the separation between the orange and purple dashed lines, is less than that exhibited by the experimental data. Therefore, this comparison of the oxygen-fugacity dependence of the strain rate also suggests that deformation of olivine aggregates occurs closer to the isostress endmember than the isostrain endmember. Although previous work has suggested that the temperature dependence of experimental strain rates better matches those predicted by an isostrain model than those predicted by an isostress model (Hansen et al., 2016), Figure 3 demonstrates that the temperature dependences of these endmember models are sufficiently similar to not provide a robust additional discriminator.

To explore the extent to which intragranular hardening by dislocation interactions can account for the magnitude of viscosity evolution during transient creep, we perform a similar comparison between model predictions and data collected on dunites (Keefner et al., 2011), but instead consider strain rates at the onset of deformation. The red curves in Figures 2a and 2b indicate initial strain rates predicted by a plasticity flow law describing dislocation glide at high temperatures in the absence of intragranular hardening (Breithaupt et al., 2023). The dunites typically have initial dislocation densities (Jung et al., 2020) on the order of 8×10^{11} m^{-2}. As such, the red curves are predictions based on this dislocation density. We assume that these preexisting dislocations in the dunite cored for experiments are unlikely to coincidentally be organized and oriented in such a way that their stress fields systematically counteract the specific direction of the maximum principal stress applied during experiments, that is they generate negligible back stress during the initial increment of deformation. The predicted strain rates are one to two orders of magnitude faster than those modeled or measured at steady state. For comparison, the red data points indicate the initial strain rates measured in experiments on dunites at the onset of deformation before any hardening had occurred. Again, the initial strain rates predicted by the isostress model are in broad agreement with the data measured on dunites. The arrows in Figure 2b link data points representing the initial and steady-state stresses during individual experiments conducted at constant strain rate. These arrows indicate that the transients involved increases in stress that were similar in magnitude to the difference between the isostress models that omit (red) or include (black) the effects on intragranular hardening.

In contrast to the isostress model, transients predicted by the isostrain model are inconsistent with the experimental data. Conveniently, the initial strain rates predicted by the isostrain model are equivalent to those predicted by the isostress model as no intergranular stress transfer has occurred prior to the first increment of deformation. Previous formulations of the isostrain model (Karato, 1998, 2021) have assumed that intragranular processes make a negligible contribution to transients and therefore that the isostrain model should be expressed using flow laws for each slip system calibrated at steady state. In this case, the initial strain rates would be those indicated by the solid black curves in Figures 2a and 2b and would be too slow compared to strain rates measured at the onset of deformation indicated by red data points.

Lastly, we note that the oxygen fugacity (i.e., the nickel-nickel oxide buffer) in Figure 2a is that at which the flow law for dislocation glide (Breithaupt et al., 2023) was calibrated, whereas that in Figure 2b (i.e., the iron-wüstite buffer) is approximately three orders of magnitude lower to allow comparison with several more initial strain rates measured from dunites. The agreement between predicted and measured strain rates before any hardening (red curves and data in Figure 2b), even at this lower oxygen fugacity, suggests that rates of dislocation glide may have little or no dependence on oxygen fugacity.

Figure 2. Strain rates measured in experiments and predicted by the isostress and isostrain models. (a) Measured and modeled strain rates. Black circles are strain rates measured during steady-state flow (Keefner et al., 2011) normalized to a temperature of 1,250°C and oxygen fugacity of 5×10^{-3} Pa at the nickel-nickel oxide buffer. The blue line is the flow law of Keefner et al. (2011) that they originally fit to the data. The solid black lines indicate strain rates predicted by the isostress model using flow laws measured from single crystals undergoing steady-state flow, which inherently incorporate the effects of intragranular hardening (Bai et al., 1991). The dashed black lines indicate strain rates predicted by the isostrain model, also using flow laws measured from single crystals undergoing steady-state flow, which represents hardening due to elastic interactions among grains with different orientations. In each case, the heavy line indicates strain rates predicted based on the crystallographic preferred orientation (CPO) of Åheim dunite (Figure 1) and the fine line indicates strain rates predicted based on 10^5 random crystal orientations lacking a CPO. The red curve indicates strain rates predicted by a flow law for dislocation glide (Breithaupt et al., 2023) in the absence of hardening (i.e., transient strain rates at the start of deformation) for an initial dislocation density of 8×10^{11} m^{-2}, which is representative of dislocation densities in Åheim dunite (Jung et al., 2020). The red datum is a strain rate measured at the onset of deformation before hardening (Keefner et al., 2011). (b) The same as (a) but at a temperature of 1,200°C and oxygen fugacity of 3×10^{-6} Pa at the iron-wüstite buffer to allow comparison of the models to the initial (red squares) and steady-state (black squares) strain rates measured in additional experiments (Chopra & Paterson, 1981, 1984; Doukhan et al., 1984). Arrows link data from the same experiment to indicate the evolution of stress during the transients. Uncertainties on data points are typically similar to the marker size. (c) The same as (a) but indicating the strain-rate contribution of each slip system to the isostress model based on the CPO of Åheim dunite.

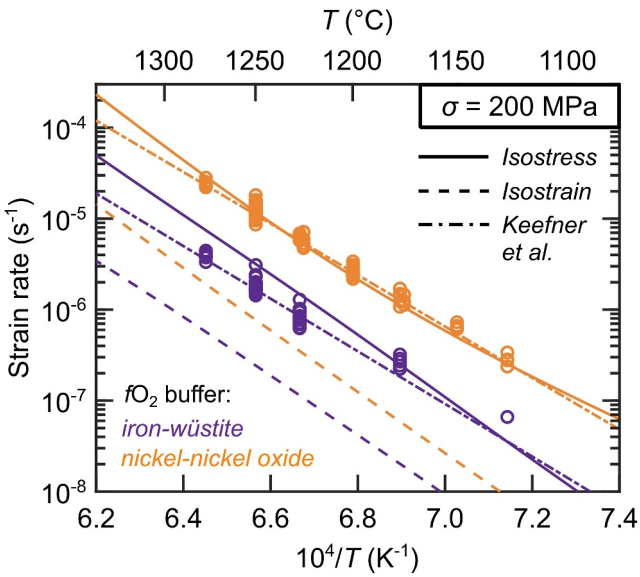

Figure 3. Strain rates measured in experiments and predicted by the isostress and isostrain models as a function of inverse temperature for both iron-wüstite (purple) and nickel-nickel oxide (orange) oxygen-fugacity buffers. Experimental data are normalized to a single stress of 200 MPa using a stress exponent of 3.5 (Bai et al., 1991). The flow law fitted by Keefner et al. (2011) is plotted as a dot-dashed line. Strain rates predicted by the isostress model are plotted as solid lines and those predicted by the isostrain model are plotted as dashed lines.

4. Discussion

4.1. Microstructural Evidence for Deformation Near the Isostress Endmember

Our interpretation that the deformation of olivine aggregates occurs close to the isostress endmember can be tested against measurements of the variation in dislocation density with grain orientation. As dislocation density is expected to be proportional to the square of resolved shear stress during steady-state creep (Bai & Kohlstedt, 1992; Breithaupt et al., 2023; Hirth & Kohlstedt, 2015), the isostress model predicts that grains in orientations that are calculated to have high resolved shear stress on the easy slip system will exhibit greater dislocation densities than grains in which the resolved shear stress is lower. In contrast, the isostrain model predicts that stress is transferred away from grains that are well oriented for the easy slip system and the stress is instead supported by grains in other orientations. Therefore, the isostrain model predicts that this latter population of grains should in fact support greater than average stresses and exhibit greater than average dislocation densities.

Measurements of the variation in dislocation density with grain orientation demonstrate that grains that are well oriented for the easy slip system do exhibit greater dislocation densities than grains that are badly oriented for the easy slip system (Farla et al., 2011; Karato, 1988; Karato & Lee, 1999; Lee et al., 2002). Karato (1988) measured the orientations and dislocation densities of grains of olivine in an aggregate deformed in axisymmetric compression at a temperature of 1,300°C. In this data set, the relative average Schmid factors of populations of grains can be inferred from visual inspection of pole figures. Grains with dislocation densities that were less than average typically occupied orientations with low resolved shear stress on the easy slip system and vice versa (Figures 4d and 4e of Karato, 1988). Lee et al. (2002) presented a similar set of results from samples deformed in simple shear, supported by quantification of Schmid factors for the (010)[100] slip system in the inverse pole figure (Figures 2, 4, and 6 of Lee et al., 2002). Karato and Lee (1999) expanded the observational base to include wet and dry aggregates deformed at a temperature of 1,300°C and a dry single crystal deformed until it underwent dynamic recrystallization to form an aggregate at 1,600°C. This data set included quantitative measurements of the Schmid factors for the (010)[100] and (001)[100] slip systems. For example, in sample MIT-5, dislocation density increased from approximately 10^{11} m^{-2} in grains with Schmid factors <0.01 for the (010)[100] slip system to approximately 2×10^{12} m^2 for grains with Schmid factors approaching 0.5 (Figure 7 of Karato & Lee, 1999). Farla et al. (2011) performed similar analyses but based on a larger data set of grain orientations obtained by EBSD and concluded that "for coarser-grained San Carlos olivine, there is strong evidence from all analyses that grains of high dislocation density are favorably orientated to deform via the slip system (010)[100], but probably with important contributions from other slip systems." Therefore these observations indicate that deformation of olivine aggregates occurs closer to the isostress endmember than the isostrain endmember.

The same phenomenon can be probed indirectly by analysis of olivine aggregates that have been deformed and have subsequently undergone partial static annealing by abnormal grain growth. Abnormal grain growth is a process whereby a small subset of grains grow preferentially by consuming their neighbors. This preferential growth of a subset of grains can result from one or both of two potential causes. First, differences in the density of dislocations and their stored energy between adjacent grains can cause preferential growth of those grains that have lower dislocation densities than their neighbors. Second, differences in the mobility of grain boundaries due to the misorientation characteristics and/or boundary planes may cause preferential growth of grains with particular relationships to their neighbors. Therefore, observation of the grains that grow preferentially during static annealing indicates that those grains had lower preexisting dislocation densities and/or more mobile grain boundaries than average.

Such observations have been made of olivine aggregates that have been deformed in geometries with a dominant component of simple shear and subsequently subjected to partial static annealing (Boneh et al., 2017, 2021).

During deformation in simple shear, grains reorient and form a CPO that results in high resolved shear stress on the easy slip system in the majority of grains (e.g., Hansen et al., 2016). During subsequent static annealing of olivine, grains with orientations that lie outside the CPO grow preferentially at the expense of grains within the CPO (Boneh et al., 2017, 2021). For example, in deformed synthetic samples with a CPO controlled by the weak (010)[100] slip system, with (010) aligned with the shear plane and [100] aligned with the shear direction, subsequent static annealing results in preferential growth of the subset of grains in orientations that are different to this initial CPO (Figures 1–3 of Boneh et al., 2017). The same effect is recorded in xenoliths from the Wyoming Craton (Boneh et al., 2021). These xenoliths contain a matrix of finer-grained olivine that exhibits a CPO similar to that of the synthetic samples. This matrix is overprinted by undeformed tablet-shaped grains inferred to have grown during static annealing. Many of these tablet-shaped grains are misoriented from the CPO of the deformed matrix (Figure 6 of Boneh et al., 2021). Importantly, the abnormality of static grain growth in the deformed synthetic samples is more pronounced than grain growth during isostatic hot pressing of undeformed olivine aggregates. In these undeformed materials, relative to deformed samples, CPO is weak so many grain-boundary planes and misorientations are present, and dislocation densities are low and homogeneous so variations in the driving force for grain-boundary migration are minimal. As such, isostatic hot pressing of undeformed olivine aggregates represents a case in which the effect of variation in boundary mobility has high potential to be expressed. Therefore, the observation that static grain growth in deformed olivine aggregates is more abnormal than that in undeformed aggregates suggests that variation in dislocation density between grains is the dominant cause of abnormality in the deformed aggregates. Taken together with the fact that it is grains with orientations that lie outside the CPO that grow preferentially, these observations suggest that grains with orientations within the CPO and thus with high resolved shear stress on the easy slip system had greater dislocation densities than those with orientations outside the CPO. This interpretation is consistent with the direct observations of variation in dislocation density with grain orientation described above. Therefore the characteristics of abnormal grain growth during static annealing also imply that deformation occurs closer to the isostress endmember than the isostrain endmember and, as it occurs in both experimental (Boneh et al., 2017) and natural (Boneh et al., 2021) samples, imply that deformation under natural conditions is also close to isostress.

Lastly, the spectrum of isostress to isostrain behaviors has been considered in models that predict the evolution of CPO with strain. Whilst the range of effects and processes that can potentially impact CPO evolution with strain are diverse and complex (e.g., the relative strengths of slip systems and their strain hardening, dynamic recrystallization and grain-size reduction, and choices of model formalism), some broad trends are apparent. Tommasi et al. (2000) compared predictions of viscoplastic self-consistent models to CPOs from experiments and found that relaxing the strain-compatibility constraints away from the isostrain endmember progressively improved the predictions of CPO orientation and strength with strain (Figures 4 and 8 of Tommasi et al., 2000). The finding that isostrain models give poor predictions of CPO evolution and that relaxation of strain-compatibility constraints is required has been reproduced in subsequent studies (Boneh et al., 2015; Signorelli & Tommasi, 2015). Therefore, modeling of CPO evolution with strain broadly supports the contention that olivine aggregates do not deform at the isostrain endmember.

4.2. Intergranular Strain Compatibility by Intragranular Strain Heterogeneity

The fact that experimental strain rates are in agreement with those predicted by the isostress model indicates that strain compatibility among adjacent grains is not achieved by significant transfer of stress in a systematic manner between subpopulations of grains with different orientations. Alternatively, strain compatibility can be achieved by gradients in plastic strain (Goetze, 1978; Paterson, 1969), which are marked by the presence of geometrically necessary dislocations (Ashby, 1970; Fleck et al., 1994). As geometrically necessary dislocations are ubiquitous in deformed olivine aggregates (Wallis et al., 2019, 2021, 2022), we suggest that heterogeneous plastic strain allows olivine aggregates to deform close to the isostress endmember. To investigate the generality of this behavior, we consider the impact of each of these strain-compatibility mechanisms on the energy budget of deformation. If the difference in strain between a grain and the bulk is $\Delta\varepsilon$, then strain compatibility can be maintained by transferring a stress $\mu\Delta\varepsilon$ to or away from the grain. The excess elastic energy stored by this mechanism is $(1/2)\mu(\Delta\varepsilon)^2$. Alternatively, this strain difference can be accommodated by gradients in plastic strain, resulting in a density of geometrically necessary dislocations given by $\rho_{\mathrm{GND}} = |\Delta\varepsilon|/(4bd)$ (Ashby, 1970). The stored energy associated with the stress fields of these dislocations is $(1/2)\mu b^2\rho_{\mathrm{GND}} = (1/8)\mu(b/d)|\Delta\varepsilon|$ (Hull & Bacon, 2011). Crucially, the energy stored by dislocations is linear in

the strain difference, whereas the energy stored by elastic stress transfer is quadratic in this quantity. Thus, for strain differences exceeding a critical value, $b/(4d)$, it is more energetically favorable to maintain strain compatibility by gradients in plastic strain, with associated geometrically necessary dislocations, than by further stress transfer. For the grain size of 0.9 mm used in the experiments (Keefner et al., 2011) considered in Figures 2 and 3, which is comparable to those in much of the upper mantle (e.g., Ave Lallemant et al., 1980; Behr & Hirth, 2014), the critical strain difference is approximately 10^{-7}, which corresponds to a total transferred stress of only approximately 10 kPa. This predicted transferred stress is orders of magnitude less than differential stresses applied in the laboratory (e.g., Keefner et al., 2011) and differential stresses that are inferred to operate in regions of deforming mantle (e.g., Ave Lallemant et al., 1980; Behr & Hirth, 2014; Hansen & Warren, 2015). Consequently, systematic stress transfer among grains with different lattice orientations, which is part of the isostrain model, seems unlikely to make a significant contribution to deformation in either the laboratory or the mantle.

Whilst we have focussed on grain size-insensitive dislocation creep to allow a straightforward comparison of strain rates measured on single crystals to those measured on aggregates, the grain-size sensitive mechanism of dislocation-accommodated grain-boundary sliding (disGBS) is also likely important in the upper mantle (Hansen et al., 2011). The analysis of Breithaupt et al. (2023) suggests that disGBS is simply a form of dislocation creep in which strain rate increases with decreasing grain size due to enhanced recovery facilitated by diffusion of point defects along grain boundaries. As such, whilst it is more practicable to assess isostrain or isostress behaviors in grain size-insensitive dislocation creep, we suggest that the isostress result of this assessment is likely also applicable to disGBS. Olivine deformed by disGBS also exhibits ubiquitous geometrically necessary dislocations (Wallis et al., 2019, 2021) that mark the intragranular strain gradients that maintain intergranular strain compatibility. Furthermore, any sliding on grain boundaries (e.g., Hansen et al., 2011) or enhanced diffusion along grain boundaries (Breithaupt et al., 2023) in disGBS provide additional mechanisms to maintain strain compatibility and promote isostress behavior.

4.3. Implications for Steady-State Dislocation Creep

To explore the implications of discriminating between the isostress and isostrain endmembers of dislocation creep for steady-state flow in the upper mantle, we analyze the ratio of viscosities predicted by each endmember model as a function of temperature and oxygen fugacity as presented in Figure 4. We note that these ratios are independent of differential stress as the stress sensitivities of each slip system are identical. Whilst the strain rates, and hence viscosities, predicted by the isostress and isostrain models differ by approximately one order of magnitude under the high temperatures and relatively low pressures of laboratory experiments (Figures 2 and 3), this difference increases to two or three orders of magnitude at the lower temperatures and higher pressures typical of the shallow upper mantle (Figure 4). This effect is controlled primarily by the different temperature dependencies of the slip systems that exert the dominant control on strain rate in each model. The difference between the viscosities predicted by each model is particularly pronounced under the low temperatures and high oxygen fugacities typical of the shallow portions of subduction zones. This difference is important because the observations and analyses described above demonstrate that the leading conventional flow law for coarse-grained olivine (Keefner et al., 2011), calibrated against data from aggregates and taking the power-law form that is typically incorporated in geodynamic models, is essentially a simplified representation of the behavior of an isostress material and may be broadly appropriate. In contrast, isostrain models (e.g., Karato, 1998, 2021; Masuti & Barbot, 2021) yield viscosities that are orders of magnitude more viscous than the isostress model under mantle conditions and provide an inappropriate conceptual basis for models of flow in subduction zones.

4.4. Implications for Transient Dislocation Creep

We can assess the significance of discriminating between isostress and isostrain models in the context of transient creep by comparing the predictions of more complex models that explicitly include the evolution of viscosity with strain/time due to either dislocation interactions, which are assumed to be the dominant cause of hardening in an isostress material, or grain interactions, which are assumed to dominate hardening in an isostrain material. As an example, we explore transient viscosity evolution of the upper mantle in a simplified postseismic scenario using the dislocation-interaction model of Breithaupt et al. (2023) (Section 2.4.2) and the grain-interaction model of Karato (2021) (Section 2.4.1).

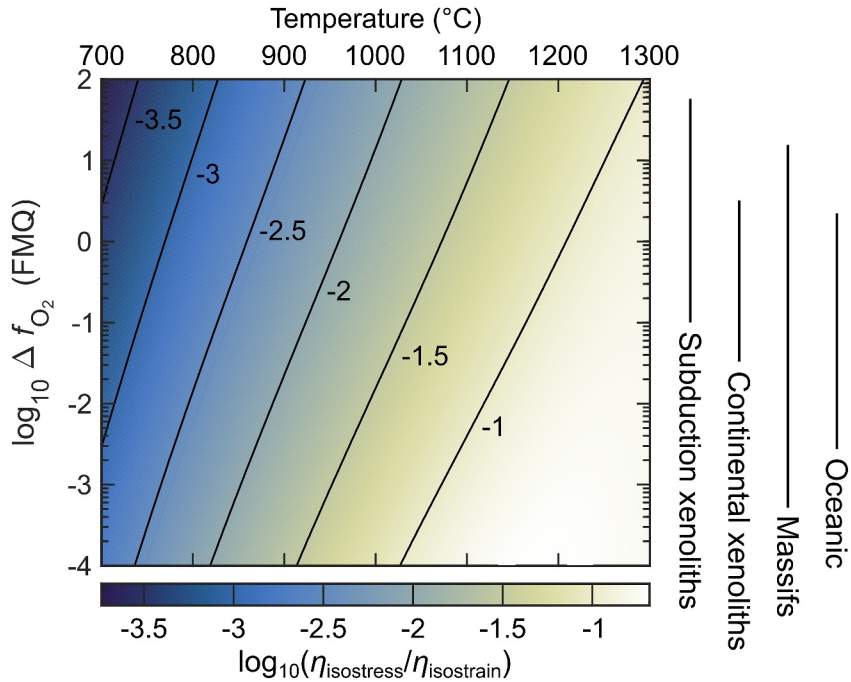

Figure 4. The ratio of steady-state viscosities predicted by the isostress ($\eta_{isostress}$) and isostrain ($\eta_{isostrain}$) models as a function of temperature and oxygen fugacity (f_{O_2}) over ranges relevant to the upper mantle. Oxygen fugacities and strain rates were calculated as functions of temperature at a pressure of 3.3 GPa corresponding to a depth of approximately 100 km. Oxygen fugacities are reported relative to that at the fayalite-magnetite-quartz buffer. The vertical bars on the right indicate the ranges of oxygen fugacities estimated from mantle rocks exhumed as subduction-zone xenoliths, continental xenoliths, orogenic peridotite massifs, and oceanic peridotites (D. J. Frost & McCammon, 2008).

To approximate postseismic deformation, we set up a simple zero-dimensional model with an initial, background stress of 0.1 MPa representing typical interseismic stress in the mantle wedge below a locked portion of a subduction interface (e.g., Govers et al., 2018; Sobolev & Muldashev, 2017). For both models, we integrate internal-stress changes until strain rate and internal stress reach the steady-state values associated with the applied macroscopic interseismic stress. Then, we impose a step increase in stress, representing the increase in stress in the upper mantle below a coseismic rupture, and keep this stress constant for the remaining time. Here, we integrate internal-stress changes until a new steady-state strain rate is reached. Whilst postseismic deformation in nature likely involves more complex stress histories, such as stress relaxation, this simplified scenario allows a transparent comparison of model behaviors for the simple purpose of highlighting similarities and significant differences.

Figure 5a presents the evolution of viscosity predicted by the models based on either dislocation interactions or grain interactions in the aftermath of two example stress changes. After the stress increase, both models predict strain rates that are higher, and hence viscosities that are lower, than those at eventual steady state. The model based on dislocation interactions predicts reductions in viscosity over timescales on the order of 10^1–10^2 days, driven by increases in the number of dislocations, followed by viscosity increase over similar intervals, due to increasing back stress from dislocation interactions. In contrast, the model based on grain interactions predicts that the viscosity minimum occurs immediately after the stress change and is followed by a gradual monotonic increase in viscosity over 10^3–10^4 days.

To assess the typical viscosity magnitudes of the transients, Figure 5b presents the ratio of the minimum viscosity to the steady-state viscosity over final stresses in the range 0.1–1 MPa and temperatures in the range 1,250–1,400°C. The viscosity ratios are fairly insensitive to final stress and temperature over these ranges and are on the order of 10^{-2} for the model based on dislocation interactions and 10^{-1} for the model based on grain interactions. The magnitudes of viscosity change of approximately two orders of magnitude predicted based on dislocation interactions are broadly similar to those inferred from postseismic geodetic time series after, for example, the

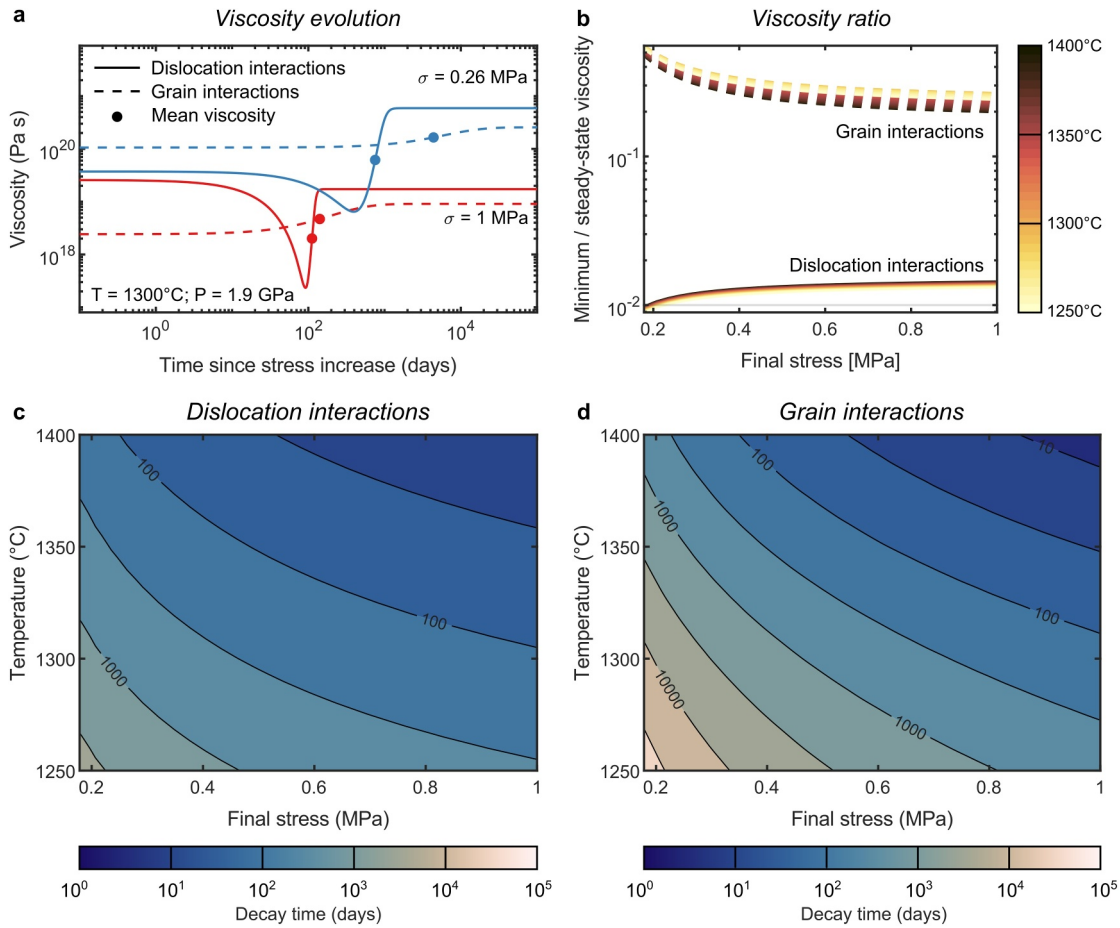

Figure 5. Predictions of viscosity evolution from models of dislocation interactions and grain interactions. Starting from an initial stress of 0.1 MPa, we increase the stress to a new constant stress over a range of stresses and temperatures and compute the viscosity evolution using models of dislocation interactions (Breithaupt et al., 2023) and grain interactions (Karato, 2021). In the model of grain interactions, we use flow laws for the weak (010)[100] and strong (010)[001] slip systems (Bai et al., 1991). (a) The evolution of viscosity for both models, at a temperature of 1,300°C and a pressure corresponding to 60 km depth, for two different final stresses. The dot denotes the reference viscosity, defined as the geometric mean of the minimum and steady-state viscosities, for each curve used to determine the decay times illustrated in (c) and (d). (b) The ratio between minimum viscosity after the stress increase and the subsequent steady-state viscosity as a function of final stress for a range of temperatures. (c) The decay time that it takes for viscosity to increase to the reference viscosity in the model of dislocation interactions. (d) The decay time that it takes for viscosity to increase to the reference viscosity in the model of grain interactions.

2012 M_w 8.6 Indian Ocean earthquake (Masuti et al., 2016) or the 2011 M_w 9.0 Tōhoku earthquake (Muto et al., 2019).

To characterize the typical durations of the transients, we define a decay time, representing the time that it takes for the viscosity to return to an intermediate reference viscosity, η_{ref}, that we define as the geometric mean of the minimum, η_{min}, and steady-state, $\eta_{steady-state}$, viscosities ($\eta_{ref} = \sqrt{\eta_{min} \cdot \eta_{steady-state}}$), which is useful when viscosities change by multiple orders of magnitude. Points on the curves in Figure 5a mark this geometric mean viscosity on the viscosity-time series. Figures 5c and 5d present the decay times as functions of final stress and temperature predicted by the models based on dislocation interactions and grain interactions respectively over the same ranges as Figure 5b. Decay times predicted by the model based on dislocation interactions are typically on the order of 10^1–10^2 days whereas those predicted by the model based on grain interactions span a wider range of approximately 10^1–10^4 days. These decay times are broadly consistent with those implied by postseismic geodetic data, which are typically on the order of 10^2–10^3 days (e.g., Broerse et al., 2015; Freed et al., 2012, 2017; Masuti et al., 2016; Muto et al., 2019; Peña et al., 2020), but do not provide a strong discriminator between the relevance of the two models.

These order-of-magnitude contrasts in the magnitude and duration of viscosity evolution during transient creep predicted by the models based on dislocation interactions and grain interactions demonstrates the importance of discriminating between the isostress and isostrain material behaviors with which each of these models of transient creep is respectively associated. Our finding that the rheological behavior of olivine aggregates matches that predicted by the isostress endmember indicates that transient creep occurs primarily due to dislocation interactions, rather than the grain interactions associated with the isostrain endmember. Alongside the inferences from mechanical data in this study and previous work (e.g., Breithaupt et al., 2023; Hansen et al., 2021), the prominent role of dislocation interactions in transient dislocation creep of olivine is supported by microstructural observations of changes in dislocation density and the stress fields of dislocations (Durham & Goetze, 1977; Hansen et al., 2021; Hanson & Spetzler, 1994; Wallis et al., 2017, 2021, 2022; Wiesman et al., 2024). For example, dislocation density evolves during transient creep in both single crystals of olivine (Durham & Goetze, 1977; Hanson & Spetzler, 1994), which have no neighboring grains to interact with, and in aggregates (Wiesman et al., 2024). These changes in dislocation density modify both the number of dislocations available to generate strain (e.g., Breithaupt et al., 2023; Hansen et al., 2021) and the intensity of elastic interactions that modulate their mobility (e.g., Wallis et al., 2017, 2021, 2022; Wiesman et al., 2024). The analysis in Figure 5 suggests that, under conditions typical of the upper mantle, the transients arising from dislocation interactions involve greater viscosity changes, are briefer in duration, and are more complex in form than those predicted by the isostrain model that forms the conceptual basis of recent analyses of postseismic geodetic data (Masuti et al., 2016; Muto et al., 2019). Overall, this simplified example demonstrates the importance of our results in discriminating the most appropriate model to employ in analyses of postseismic deformation as the different models predict significantly different rheological behaviors.

Lastly, we note that several previous works have represented transient creep of olivine by fitting phenomenological models, such as Burgers models, to experimental data (Chopra, 1997; Hanson & Spetzler, 1994; Masuti & Barbot, 2021; Ohuchi et al., 2024; Post, 1977; Smith & Carpenter, 1987). Such fitting exercises may generate equations that superficially reproduce some aspects of the behaviors observed under the conditions of a particular set of experiments. However, even if a close fit is obtained, two important points must be borne in mind in relation to the applicability of such models to analysis of deformation in Earth's interior. First, the lack of a robust microphysical basis to these models means that extrapolation beyond their calibration range does not necessarily yield accurate predictions of deformation behaviors. Rather, the interactions among underlying physical processes (e.g., rates of dislocation glide and climb) may play out differently in Earth's interior due to their different dependencies on stress, temperature, and other factors, potentially leading to significantly different behaviors (e.g., Paterson, 1976). As such, we reiterate the long-standing point that the development of models that capture the important microphysics should take precedence over cursory fitting of phenomenological equations (e.g., Paterson, 1976). Second, although the concept of grain interactions has been linked to Burgers models as a loose, post-hoc, physical basis (Karato, 1998, 2021; Masuti & Barbot, 2021; Ohuchi et al., 2024), the finding that deformation of olivine aggregates occurs at the isostress endmember during transient and steady-state dislocation creep in laboratory experiments (Section 3), along with the microstructural and energy arguments that this is also the case in the upper mantle (Sections 4.1 and 4.2), mean that the concept of grain interactions can no longer be appealed to. Instead, modeling transient creep of olivine as occurring due to dislocation interactions (Breithaupt et al., 2023; Hansen et al., 2021) in an isostress material (Figures 2 and 3) provides a more robust microphysical approach.

5. Conclusions

Our comparison of the steady-state strain rates measured on single crystals of olivine to those measured on aggregates, properly accounting for the effects of grain orientation (Figure 1), oxygen fugacity, and pressure, demonstrates that aggregates deform at strain rates that are in excellent agreement with those predicted by the isostress model but about an order of magnitude faster than those predicted by the isostrain model (Figures 2 and 3). Unlike the isostrain model, the isostress model also well predicts the magnitude of strain hardening observed in laboratory experiments (Figure 2). When extrapolated to conditions typical of the upper mantle, the steady-state strain rates predicted by the isostress and isostrain models (Figure 4), along with the magnitudes, durations, and forms of transients resulting from associated microphysical processes (Figure 5), all differ by orders of magnitude. These results challenge theoretical work (Karato, 1998, 2021; Masuti & Barbot, 2021; Masuti et al., 2019) and recent analyses of geodetic data (Masuti et al., 2016; Muto et al., 2019) that either explicitly or implicitly

assume a priori that olivine aggregates deform close to the isostrain endmember with transients arising from stress transfer between soft and hard slip systems in grains of different orientation. Instead, laboratory data demonstrate that olivine aggregates deform close to the isostress endmember, which we suggest is possible primarily due to the occurrence of heterogeneous intragranular strain fields associated with geometrically necessary dislocations. As such, recent models for transient and steady-state plasticity and dislocation creep of olivine aggregates (Breithaupt et al., 2023; Hansen et al., 2019, 2021), in which viscosity is controlled by the density of dislocations and the strength of interactions among them, provide a more robust physical basis for analyzing the rheological behavior of the upper mantle.

Data Availability Statement

Supporting Information includes Tables S1 and S2 in Supporting Information S1. The code and data used in this paper are provided by Wallis et al. (2024).

Acknowledgments
The authors thank Lars Hansen for helpful conversations and David Kohlstedt for supplying the sample of Åheim dunite. The authors acknowledge funding from the Netherlands Organization for Scientific Research, User Support Programme Space Research Grant ALWGO.2018.038. to David Wallis and Taco Broerse and Grant ENW.GO.001.005 to Taco Broerse, David Wallis, and Thomas Breithaupt. David Wallis acknowledges funding from a UK Research and Innovation Future Leaders Fellowship MR/V021788/1. Thomas Breithaupt acknowledges funding from a Research Fellowship from the Royal Commission for the Exhibition of 1851.

References

Abramson, E. H., Brown, J. M., Slutsky, L. J., & Zaug, J. (1997). The elastic constants of San Carlos olivine to 17 GPa. *Journal of Geophysical Research*, *102*, 12253–12263. https://doi.org/10.1029/97JB00682

Ashby, M. F. (1970). The deformation of plastically non-homogeneous materials. *Philosophical Magazine*, *21*(170), 399–424. https://doi.org/10.1080/14786437008238426

Ashby, M. F., & Duval, P. (1985). The creep of polycrystalline ice. *Cold Regions Science and Technology*, *11*(3), 285–300. https://doi.org/10.1016/0165-232X(85)90052-7

Ave Lallemant, H. G., Mercier, J.-C., Carter, N. L., & Ross, J. V. (1980). Rheology of the upper mantle: Inferences from peridotite xenoliths. *Tectonophysics*, *70*(1–2), 85–113. https://doi.org/10.1016/0040-1951(80)90022-0

Bai, Q., & Kohlstedt, D. L. (1992). High-temperature creep of olivine single crystals, 2. Dislocation structures. *Tectonophysics*, *206*(1–2), 1–29. https://doi.org/10.1016/0040-1951(92)90365-D

Bai, Q., Mackwell, S. J., & Kohlstedt, D. L. (1991). High-temperature creep of olivine single crystals 1. Mechanical results for buffered samples. *Journal of Geophysical Research*, *96*(B2), 2441–2463. https://doi.org/10.1029/90JB01723

Ballhaus, C., Berry, R. F., & Green, D. H. (1991). High pressure experimental calibration of the olivine-orthopyroxene-spinel oxygen geobarometer: Implications for the oxidation state of the upper mantle. *Contributions to Mineralogy and Petrology*, *107*(1), 27–40. https://doi.org/10.1007/BF00311183

Behr, W. M., & Hirth, G. (2014). Rheological properties of the mantle lid beneath the Mojave region in southern California. *Earth and Planetary Science Letters*, *393*, 60–72. https://doi.org/10.1016/j.epsl.2014.02.039

Boneh, Y., Chin, E. J., Chilson-Parks, B. H., Saal, A. E., Hauri, E. H., Hearn, B. C., & Hirth, G. (2021). Microstructural shift due to post-deformation annealing in the upper mantle. *Geochemistry, Geophysics, Geosystems*, *22*(3), e2020GC009377. https://doi.org/10.1029/2020GC009377

Boneh, Y., Morales, L. F. G., Kaminski, E., & Skemer, P. (2015). Modeling olivine CPO evolution with complex deformation histories: Implications for the interpretation of seismic anisotropy in the mantle. *Geochemistry, Geophysics, Geosystems*, *16*(10), 3436–3455. https://doi.org/10.1002/2015GC005964

Boneh, Y., Wallis, D., Hansen, L. N., Krawczynski, M. J., & Skemer, P. (2017). Oriented grain growth and modification of 'frozen anisotropy' in the lithospheric mantle. *Earth and Planetary Science Letters*, *474*, 368–374. https://doi.org/10.1016/j.epsl.2017.06.050

Breithaupt, T., Katz, R. F., Hansen, L. N., & Kumamoto, K. M. (2023). Dislocation theory of steady and transient creep of crystalline solids: Predictions for olivine. *Proceedings of the National Academy of Sciences*, *120*(8), e2203448120. https://doi.org/10.1073/pnas.2203448120

Broerse, T., Riva, R., Simons, W., Govers, R., & Vermeersen, B. (2015). Postseismic GRACE and GPS observations indicate a rheology contrast above and below the Sumatra slab. *Journal of Geophysical Research: Solid Earth*, *120*(7), 5343–5361. https://doi.org/10.1002/2015JB011951

Castelnau, O., Blackman, D. K., Lebensohn, R. A., & Ponte Castañeda, P. (2008). Micromechanical modeling of the viscoplastic behavior of olivine. *Journal of Geophysical Research*, *113*(B9), B09202. https://doi.org/10.1029/2007JB005444

Chopra, P. N. (1997). High-temperature transient creep in olivine rocks. *Tectonophysics*, *279*(1–4), 93–111. https://doi.org/10.1016/S0040-1951(97)00134-0

Chopra, P. N., & Paterson, M. S. (1981). The experimental deformation of dunite. *Tectonophysics*, *78*(1–4), 453–473. https://doi.org/10.1016/0040-1951(81)90024-X

Chopra, P. N., & Paterson, M. S. (1984). The role of water in the deformation of dunite. *Journal of Geophysical Research*, *89*(B9), 7861–7876. https://doi.org/10.1029/JB089iB09p07861

Cooper, R. F., Stone, D. S., & Plookphol, T. (2016). Load relaxation of olivine single crystals. *Journal of Geophysical Research: Solid Earth*, *121*(10), 7193–7210. https://doi.org/10.1002/2016JB013425

Dixon, N. A., & Durham, W. B. (2018). Measurement of activation volume for creep of dry Olivine at upper-mantle conditions. *Journal of Geophysical Research: Solid Earth*, *123*(10), 8459–8473. https://doi.org/10.1029/2018JB015853

Doukhan, N., Doukhan, J. C., Fitz Gerald, J. D., Chopra, P. N., & Paterson, M. S. (1984). A TEM microstructural study of experimentally deformed Anita Bay dunite. In R. E. Tressler & R. C. Bradt (Eds.), *Deformation of ceramic materials II* (pp. 307–319). Springer. https://doi.org/10.1007/978-1-4615-6802-5_20

Durham, W. B., Froidevaux, C., & Jaoul, O. (1979). Transient and steady-state creep of pure forsterite at low stress. *Physics of the Earth and Planetary Interiors*, *19*(3), 263–274. https://doi.org/10.1016/0031-9201(79)90027-X

Durham, W. B., & Goetze, C. (1977). Plastic flow of oriented single crystals of olivine: 1. Mechanical data. *Journal of Geophysical Research*, *82*(36), 5737–5753. https://doi.org/10.1029/JB082i036p05737

Duval, P., Ashby, M. F., & Anderman, I. (1983). Rate-controlling processes in the creep of polycrystalline ice. *Journal of Physical Chemistry*, *87*(21), 4066–4074. https://doi.org/10.1021/j100244a014

Farla, R. J. M., Fitz Gerald, J. D., Kokkonen, H., Halfpenny, A., Faul, U. H., & Jackson, I. (2011). Slip-system and EBSD analysis on compressively deformed fine-grained polycrystalline olivine. In D. J. Prior, E. H. Rutter, & D. J. Tatham (Eds.), *Deformation mechanisms,*

rheology and tectonics: microstructures, mechanics and anisotropy (Vol. 360, pp. 225–235). Geological Society, London, Special Publications. https://doi.org/10.1144/SP360.13

Fleck, N. A., Muller, G. M., Ashby, M. F., & Hutchinson, J. W. (1994). Strain gradient plasticity: Theory and experiment. *Acta Metallurgica et Materialia*, *42*(2), 475–487. https://doi.org/10.1016/0956-7151(94)90502-9

Freed, A. M. (2005). Earthquake triggering by static, dynamic, and postseismic stress transfer. *Annual Review of Earth and Planetary Sciences*, *33*(1), 335–367. https://doi.org/10.1146/annurev.earth.33.092203.122505

Freed, A. M., Bürgmann, R., Calais, E., & Freymueller, J. (2006). Stress-dependent power-law flow in the upper mantle following the 2002 Denali, Alaska, earthquake. *Earth and Planetary Science Letters*, *252*(3–4), 481–489. https://doi.org/10.1016/j.epsl.2006.10.011

Freed, A. M., Hashima, A., Becker, T. W., Okaya, D. A., Sato, H., & Hatanaka, Y. (2017). Resolving depth-dependent subduction zone viscosity and afterslip from postseismic displacements following the 2011 Tohoku-oki, Japan earthquake. *Earth and Planetary Science Letters*, *459*, 279–290. https://doi.org/10.1016/j.epsl.2016.11.040

Freed, A. M., Herring, T., & Bürgmann, R. (2010). Steady-state laboratory flow laws alone fail to explain postseismic observations. *Earth and Planetary Science Letters*, *300*(1–2), 1–10. https://doi.org/10.1016/j.epsl.2010.10.005

Freed, A. M., Hirth, G., & Behn, M. D. (2012). Using short-term postseismic displacements to infer the ambient deformation conditions of the upper mantle. *Journal of Geophysical Research*, *117*(B1), B01409. https://doi.org/10.1029/2011JB008562

Frost, B. R. (1991). Stability of oxide minerals in metamorphic rocks. *Reviews in Mineralogy and Geochemistry*, *25*, 469–488.

Frost, D. J., & McCammon, C. A. (2008). The redox state of Earth's mantle. *Annual Review of Earth and Planetary Sciences*, *36*(1), 389–420. https://doi.org/10.1146/annurev.earth.36.031207.124322

Goetze, C. (1978). The mechanisms of creep in olivine. *Philosophical Transactions of the Royal Society A*, *288*, 99–119. https://doi.org/10.1098/rsta.1978.0008

Govers, R., Furlong, K. P., van de Wiel, L., Herman, M. W., & Broerse, T. (2018). The geodetic signature of the earthquake cycle at subduction zones: Model constraints on the deep processes. *Reviews of Geophysics (1985)*, *56*(1), 6–49. https://doi.org/10.1002/2017RG000586

Hansen, L. N., Conrad, C. P., Boneh, Y., Skemer, P., Warren, J. M., & Kohlstedt, D. L. (2016). Viscous anisotropy of textured olivine aggregates: 2. Micromechanical model. *Journal of Geophysical Research: Solid Earth*, *121*(10), 7137–7160. https://doi.org/10.1002/2016JB013240

Hansen, L. N., Kumamoto, K. M., Thom, C. A., Wallis, D., Durham, W. B., Goldsby, D. L., et al. (2019). Low-temperature plasticity in Olivine: Grain size, strain hardening, and the strength of the lithosphere. *Journal of Geophysical Research: Solid Earth*, *124*(6), 5427–5449. https://doi.org/10.1029/2018JB016736

Hansen, L. N., Wallis, D., Breithaupt, T., Thom, C., & Kempton, I. (2021). Dislocation creep of olivine: Backstress evolution controls transient creep at high temperatures. *Journal of Geophysical Research: Solid Earth*, *126*(5), e2020JB021325. https://doi.org/10.1029/2020JB021325

Hansen, L. N., & Warren, J. M. (2015). Quantifying the effect of pyroxene on deformation of peridotite in a natural shear zone. *Journal of Geophysical Research: Solid Earth*, *120*(4), 2717–2738. https://doi.org/10.1002/2014JB011584

Hansen, L. N., Zimmerman, M. E., & Kohlstedt, D. L. (2011). Grain boundary sliding in San Carlos olivine: Flow law parameters and crystallographic-preferred orientation. *Journal of Geophysical Research*, *116*(B8), B08201. https://doi.org/10.1029/2011JB008220

Hanson, D. R., & Spetzler, H. A. (1994). Transient creep in natural and synthetic, iron-bearing olivine single crystals: Mechanical results and dislocation microstructures. *Tectonophysics*, *235*(4), 293–315. https://doi.org/10.1016/0040-1951(94)90191-0

Hirth, G., & Kohlstedt, D. L. (2015). The stress dependence of olivine creep rate: Implications for extrapolation of lab data and interpretation of recrystallized grain size. *Earth and Planetary Science Letters*, *418*, 20–26. https://doi.org/10.1016/j.epsl.2015.02.013

Hoechner, A., Sobolev, S. V., Einarsson, I., & Wang, R. (2011). Investigation on afterslip and steady state and transient rheology based on postseismic deformation and geoid change caused by the Sumatra 2004 earthquake. *Geochemistry, Geophysics, Geosystems*, *12*(7), Q07010. https://doi.org/10.1029/2010GC003450

Hull, D., & Bacon, D. J. (2011). *Introduction to dislocations*. Butterworth-Heinemann.

Jin, Z. M., Bai, Q., & Kohlstedt, D. L. (1994). High-temperature creep of olivine crystals from four localities. *Physics of the Earth and Planetary Interiors*, *82*(1), 55–64. https://doi.org/10.1016/0031-9201(94)90102-3

Jung, S., Jung, H., & Austrheim, H. (2020). Microstructural evolution of amphibole peridotites in Åheim, Norway, and the implications for seismic anisotropy in the mantle wedge. *Minerals (Basel)*, *10*(4), 345. https://doi.org/10.3390/min10040345

Karato, S.-I. (1988). The role of recrystallization in the preferred orientation of olivine. *Physics of the Earth and Planetary Interiors*, *51*(1–3), 107–122. https://doi.org/10.1016/0031-9201(88)90029-5

Karato, S.-I. (1998). Micro-physics of post glacial rebound. In P. Wu (Ed.), *Dynamics of the ice age earth: A modern perspective* (pp. 351–364). Trans Tech Publications.

Karato, S.-I. (2021). A theory of inter-granular transient dislocation creep: Implications for the geophysical studies on mantle rheology. *Journal of Geophysical Research: Solid Earth*, *126*(10), e2021JB022763. https://doi.org/10.1029/2021JB022763

Karato, S.-I., & Lee, K.-H. (1999). Stress-strain distribution in deformed olivine aggregates: Inference from microstructural observations and implications for texture development. In *Proceedings of the twelfth international conference on textures of materials* (pp. 1546–1555). Canadian Institute of Mining, Metallurgy and Petroleum.

Keefner, J. W., Mackwell, S. J., Kohlstedt, D. L., & Heidelbach, F. (2011). Dependence of dislocation creep of dunite on oxygen fugacity: Implications for viscosity variations in Earth's mantle. *Journal of Geophysical Research*, *116*(B5), B05201. https://doi.org/10.1029/2010JB007748

Kohlstedt, D. L., & Goetze, C. (1974). Low-stress high-temperature creep in olivine single crystals. *Journal of Geophysical Research*, *79*(14), 2045–2051. https://doi.org/10.1029/JB079i014p02045

Lee, K.-H., Jiang, Z., & Karato, S.-I. (2002). A scanning electron microscope study of the effects of dynamic recrystallization on lattice preferred orientation in olivine. *Tectonophysics*, *351*(4), 331–341. https://doi.org/10.1016/S0040-1951(02)00250-0

Masuti, S., & Barbot, S. (2021). MCMC inversion of the transient and steady-state creep flow law parameters of dunite under dry and wet conditions. *Earth Planets and Space*, *73*(1), 208. https://doi.org/10.1186/s40623-021-01543-9

Masuti, S., Barbot, S. D., Karato, S.-I., Feng, L., & Banerjee, P. (2016). Upper-mantle water stratification inferred from observations of the 2012 Indian Ocean earthquake. *Nature*, *538*(7625), 373–377. https://doi.org/10.1038/nature19783

Masuti, S., Karato, S.-I., Girard, J., & Barbot, S. D. (2019). Anisotropic high-temperature creep in hydrous olivine single crystals and its geodynamic implications. *Physics of the Earth and Planetary Interiors*, *290*, 1–9. https://doi.org/10.1016/j.pepi.2019.03.002

Mei, S., & Kohlstedt, D. L. (2000). Influence of water on plastic deformation of olivine aggregates: 2. Dislocation creep regime. *Journal of Geophysical Research*, *105*(B9), 21471–21481. https://doi.org/10.1029/2000JB900180

Meyers, C., & Kohlstedt, D. L. (2021). Experimental measurements of anisotropic viscosity in naturally sourced dunite with a preexisting CPO. *Tectonophysics*, *815*, 228949. https://doi.org/10.1016/j.tecto.2021.228949

Muto, J., Moore, J. D. P., Barbot, S., Iinuma, T., Ohta, Y., & Iwamori, H. (2019). Coupled afterslip and transient mantle flow after the 2011 Tohoku earthquake. *Science Advances*, *5*(9), eaaw1164. https://doi.org/10.1126/sciadv.aaw1164

Ohuchi, T., Higo, Y., Tsujino, N., Seto, Y., Kakizawa, S., Tange, Y., et al. (2024). Transient creep in olivine at shallow mantle pressures: Implications for time-dependent rheology in post-seismic deformation. *Geophysical Research Letters*, *51*(11), e2024GL108356. https://doi.org/10.1029/2024GL108356

O'Neill, H. S. C. (1987a). Free energies of formation of NiO, CoO, Ni_2SiO_4, and Co_2SiO_4. *American Mineralogist*, *72*, 280–291.

O'Neill, H. S. C. (1987b). Quartz-fayalite-iron and quartz-fayalite-magnetite equilibria and the free energy of formation of fayalite (Fe_2SiO_4) and magnetite (Fe_3O_4). *American Mineralogist*, *72*, 67–75.

Orowan, E. (1964). Continental drift and the origin of mountains: Hot creep and creep fracture are crucial factors in the formation of continents and mountains. *Science*, *146*(3647), 1003–1010. https://doi.org/10.1126/science.146.3647.1003

Paterson, M. S. (1969). The ductility of rocks. In E. Orowan (Ed.), *Physics of strength and plasticity* (pp. 377–392). M.I.T. Press.

Paterson, M. S. (1976). Some current aspects of experimental rock deformation. *Philosophical Transactions of the Royal Society of London*, *283*, 163–172.

Peña, C., Heidbach, O., Moreno, M., Bedford, J., Ziegler, M., Tassara, A., & Oncken, O. (2020). Impact of power-law rheology on the viscoelastic relaxation pattern and afterslip distribution following the 2010 Mw 8.8 Maule earthquake. *Earth and Planetary Science Letters*, *542*, 116292. https://doi.org/10.1016/j.epsl.2020.116292

Post, R. L., Jr. (1977). High-temperature creep of Mt. Burnet dunite. *Tectonophysics*, *42*(2–4), 75–110. https://doi.org/10.1016/0040-1951(77)90162-7

Raterron, P., Girard, J., & Chen, J. (2012). Activities of olivine slip systems in the upper mantle. *Physics of the Earth and Planetary Interiors*, *200–201*, 105–112. https://doi.org/10.1016/j.pepi.2012.04.006

Sachs, G. (1928). Zur Ableitung einer Fließbedingung. *Zeitschrift des Vereines deutscher Ingeniere*, *72*, 734–736.

Signorelli, J., & Tommasi, A. (2015). Modeling the effect of subgrain rotation recrystallization on the evolution of olivine crystal preferred orientations in simple shear. *Earth and Planetary Science Letters*, *430*, 356–366. https://doi.org/10.1016/j.epsl.2015.08.018

Simon, K. M., Riva, R. E. M., & Broerse, T. (2022). Identifying geographical patterns of transient deformation in the geological sea level record. *Journal of Geophysical Research: Solid Earth*, *127*, e2021JB023693. https://doi.org/10.1029/2021/JB023693

Smith, B. K., & Carpenter, F. O. (1987). Transient creep in orthosilicates. *Physics of the Earth and Planetary Interiors*, *49*(3–4), 314–324. https://doi.org/10.1016/0031-9201(87)90033-1

Sobolev, S. V., & Muldashev, I. A. (2017). Modeling seismic cycles of great megathrust earthquakes across the scales with focus at postseismic phase. *Geochemistry, Geophysics, Geosystems*, *18*(12), 4387–4408. https://doi.org/10.1002/2017GC007230

Tackley, P. J. (2000). Mantle convection and plate tectonics: Toward an integrated physical and chemical theory. *Science*, *288*(5473), 2002–2007. https://doi.org/10.1126/science.288.5473.2002

Taylor, G. I. (1938). Plastic strain in metals. *Journal of the Institute of Metals*, *62*, 307–324.

Tielke, J. A., Hansen, L. N., Tasaka, M., Meyers, C., Zimmerman, M. E., & Kohlstedt, D. L. (2016). Observations of grain size sensitive power law creep of olivine aggregates over a large range of lattice-preferred orientation strength. *Journal of Geophysical Research: Solid Earth*, *121*(2), 506–516. https://doi.org/10.1002/2015JB012302

Tommasi, A., Mainprice, D., Canova, G., & Chastel, Y. (2000). Viscoplastic self-consistent and equilibrium-based modeling of olivine lattice preferred orientations: Implications for the upper mantle seismic anisotropy. *Journal of Geophysical Research*, *105*(B4), 7893–7908. https://doi.org/10.1029/1999JB900411

von Mises, R. (1913). Mechanik der festen Körper im plastisch-deformablen Zustand. *Nachrichten von der Gesellschaft der Wissenschaften zu Göttingen, Mathematisch-Physikalische Klasse*, *1913*, 582–592.

Wallis, D., Breithaupt, T., & Broerse, T. (2024). Code and data for "Transient and steady-state dislocation creep of olivine controlled by dislocation interactions at the isostress endmember" [Dataset]. *Apollo University of Cambridge Repository*. https://doi.org/10.17863/CAM.113429

Wallis, D., Hansen, L. N., Britton, T. B., & Wilkinson, A. J. (2017). Dislocation interactions in Olivine revealed by HR-EBSD. *Journal of Geophysical Research: Solid Earth*, *122*(10), 7659–7678. https://doi.org/10.1002/2017JB014513

Wallis, D., Hansen, L., Wilkinson, A., & Lebensohn, R. (2021). Dislocation interactions in olivine control postseismic creep of the upper mantle. *Nature Communications*, *12*(1), 3496. https://doi.org/10.1038/s41467-021-23633-8

Wallis, D., Hansen, L. N., Kumamoto, K. M., Thom, C. A., Plümper, O., Ohl, M., et al. (2020). Dislocation interactions during low-temperature plasticity of olivine and their impact on the evolution of lithospheric strength. *Earth and Planetary Science Letters*, *543*, 116349. https://doi.org/10.1016/j.epsl.2020.116349

Wallis, D., Hansen, L. N., Tasaka, M., Kumamoto, K. M., Parsons, A. J., Lloyd, G. E., et al. (2019). The impact of water on slip system activity in olivine and the formation of bimodal crystallographic preferred orientations. *Earth and Planetary Science Letters*, *508*, 51–61. https://doi.org/10.1016/j.epsl.2018.12.007

Wallis, D., Sep, M., & Hansen, L. N. (2022). Transient creep in subduction zones by long-range dislocation interactions in Olivine. *Journal of Geophysical Research: Solid Earth*, *127*(1), e2021JB022618. https://doi.org/10.1029/2021JB022618

Warren, J. M., & Hansen, L. N. (2023). Ductile deformation of the lithospheric mantle. *Annual Review of Earth and Planetary Sciences*, *51*(1), 581–609. https://doi.org/10.1146/annurev-earth-031621-063756

Wiesman, H., Breithaupt, T., Wallis, D., & Hansen, L. N. (2024). Microstructural and micromechanical evolution of olivine aggregates during transient creep. *Journal of Geophysical Research: Solid Earth*, *129*(12), e2024JB029812. https://doi.org/10.1029/2024JB029812

Zimmerman, M. E., & Kohlstedt, D. L. (2004). Rheological properties of partially molten lherzolite. *Journal of Petrology*, *45*(2), 275–298. https://doi.org/10.1093/petrology/egg089